Submitted to JGR

Progressive shape evolution of a mineral inclusion under differential stress at high temperature: Example of garnet inclusions within a granulite-facies quartzite from the Lützow-Holm Complex, East Antarctica

Atsushi Okamoto[1], Katsuyoshi Michibayashi[1]

1 Institute of Geosciences, Shizuoka University, Shizuoka, 422-8529 Japan

Abstract

[1] Interfacial tension (γ) and differential stress (σ) affect the change the shape of a mineral grain included within a crystalline host. We present a simple model that predicts the progressive change in aspect ratio of an ellipsoidal inclusion. Three processes are considered in the model: dislocation creep, interface diffusion creep, and rounding by interface diffusion. The model reveals that (1) the inclusion aspect ratio (L) evolves toward a steady-state value, (2) the time taken to achieve a steady-state aspect ratio increases with increasing grain size (R), and (3) the dominant deformation mechanism varies from diffusion creep to dislocation creep with increasing grain size.

[2] The L-R distribution pattern of garnets in a granulite-facies quartzite from the Lützow-Holm Complex, East Antarctica is compared with the model result. The aspect ratio of garnets systematically varies with respect to grain size, and the most elongate ones are of intermediate grain size. Assuming γ_{grtqtz} = 1.0 N/m, the L-R pattern of small inclusions (< 250 μm) is similar to the model predictions of 1.4×10^{-2} MPa, whereas that of coarser inclusions can not be explained by such a small differential stress. A two-stage deformation with high and low differential stresses (stage A and B) best

explains for the observed *L-R* pattern. Assuming $D_{gb,A}$ = 1.0×10^{-12}m^2/s, $D_{gb,B}$ = 1.0×10^{-11}m^2/s and σ_A = 1.0 MPa, the garnet data is fitted to a theoretical curve under conditions of $\sigma_B = 1.4\times10^{-2}$ MPa, t_A = 0.5 Myr and t_B = 14.4 Myr.

1. Introduction

[3] The diffusion of vacancies through a crystal acts to reduce the surface (interfacial) free energy and is an important control on the changing shape of mineral grains. Material scientists have investigated this process in both theory and experiment in order to understand the annealing mechanism of ceramics and metals [e.g., *Kingery et al.*, 1976]. However, there are few comparable studies in natural rocks that seek to describe textural development in the context of interfacial free energy. It is well known that the diffusion of vacancies is driven by differential stress, and various diffusion creep models (e.g. Nabarro-Herring creep and Coble creep) have been proposed to explain this process [*Nabarro*, 1948; *Herring*, 1950; *Coble*, 1963; *Poirier*, 1985]. Annealing and diffusion creep are similar in that both processes are controlled by the concentration gradient of vacancies within a crystal, and both can proceed simultaneously under stress and high temperatures.

[4] In this study, we describe the change in shape of a single mineral inclusion within a host mineral. Analyses of the inclusion-host system provide an opportunity to understand processes affecting on a mineral under differential stress at high temperature

and to constrain the physical conditions of deformation. There are three primary advantages of addressing such problems in the context of an inclusion and mineral host. First, the effect of grain-boundary migration may be negligible in the inclusion-host system, and an assumption of volume conservation is acceptable. It is therefore possible to convert strain rate to the rate of change in shape of the inclusion. Second, in contrast with polycrystalline materials, the inclusion-host system does not contain the complex interface network with triple junction grain boundaries. Third, natural rocks commonly contain numerous mineral inclusions, and this enables us to investigate the size dependence of the inclusion deformation processes within a single sample. Rounded mineral inclusions are commonly observed in high temperature metamorphic rocks, and have been explained by a surface (interfacial) tension model [*Rast*, 1965; *Vernon*, 1968; *Spry*, 1969; *Toriumi*, 1979; *Toriumi*, 1987]. However, we lack a model that can predict the grain size – grain shape distribution under conditions of differential stress. The aim of this study is to present a simple model that describes the progressive change in shape of a single crystal inclusion during deformation. The model describes both interfacial tension and differential stress simultaneously affecting the evolving shape of the

inclusion through a coupling of three processes: dislocation creep, interface diffusion creep and rounding by interface diffusion. In this study, a term of "rounding" describes a change in shape from ellipsoidal to spherical. The rounding process is caused by differences in the local curvature of an inclusion surface, and is comparable to the annealing process within polycrystalline material. The model predicts that the inclusion aspect ratio tends toward a steady state value, and that various aspect ratio (L) – grain size (R) distribution patterns reflect the magnitudes and duration of differential stress.

[5] The L-R distribution pattern of garnet inclusions from a granulite-facies quartzite is compared with the model-derived L-R curves. We show that a two-stage process involving first deformation and then static annealing is required to explain the observed L-R pattern and estimate differential stress and duration using the assumed values of the interfacial tension and the interface diffusion coefficient at the garnet-quartz boundary.

2. Deformation Model

[6] We consider a single crystalline inclusion of rotational ellipsoidal shape,

embedded in a host mineral (Fig. 1a). The shape of the inclusion changes under differential stress. As a simplest case, we consider that the inclusion is subject to a uniaxial extension in response to stress of $\sigma_1 = \sigma_2 > \sigma_3$. Compressional stress is positive and the long axis of the inclusion is oriented parallel to σ_3.

[7] The three deformation processes most likely to accommodate a change in inclusion shape are diffusion creep, rounding process and dislocation creep. Several models have been proposed to describe diffusion creep [*Nabarro*, 1948; *Herring*, 1950; *Coble*, 1963; *Poirier*, 1985]. In this study, only interface diffusion is considered, because the interface diffusion coefficient is generally 10^4 times greater than the volume-diffusion coefficient at metamorphic temperatures [*Shewmon*, 1963; *Joesten*, 1991; *Lasaga*, 1998]. Coble (1963) suggested that the concentration gradient of vacancies within a crystal is generated under differential stress, and this drives the diffusive flow of material along the interface. The process of rounding an inclusion acts to reduce the interfacial free energy. In this process, the concentration gradient of vacancies results from the difference in the stress due to the interfacial tension, reflecting the local difference in the curvature of the inclusion. Diffusion processes due

to the interfacial tension have been modeled in terms of the annealing of ceramics and metals [e.g., *Kingery et al.*, 1976]. *Toriumi* [1987] presented a model for the rounding of a mineral inclusion by interface diffusion. Both diffusion creep and rounding affect the shape development of an inclusion via the same process; interface diffusion. The third process that we consider is dislocation creep. Several constitutive equations have been proposed to describe dislocation creep [e.g., *Poirier*, 1985]. In this paper, we follow the work proposed by *Karato et al.* [1995], which is based on the creep test for a single garnet crystal.

2-1. Shape development by diffusion process

[8] We firstly derive the equation describing the shape development of a mineral inclusion by diffusion processes following *Toriumi* [1987[and *Poirier* [1985]. The concentration gradient of vacancies in the inclusion is controlled by two driving forces; differential stress ($\sigma = \sigma_1 - \sigma_3$) and interfacial tension (γ_s). Interfacial tension (N/m) is equivalent to the interfacial free energy (J/m^2) in all cases where interfacial energy is independent of the interfacial area. It is assumed that interfacial free energy is

independent of crystallographic orientation.

[9] After an advance of time, dt, the inclusion long axis, a, and the short axis, b, change to $a+da$ and $b+db$ respectively (Fig. 1b). If the inclusion volume (V_0) remains constant, we have

$$V_0 = 4\pi ab^2/3 = 4\pi (a+da)(b+db)^2/3. \quad (1)$$

In the case of $a \gg da$ and $b \gg db$,

$$db/da = - b/2a.$$

The radii of curvatures at the crests are written as follows:

$$r_1 = a^2/b, \quad r_3 = b^2/a, \quad (2)$$

where r_1 and r_3 are the short and long axial crests, respectively. The concentrations of

lattice vacancies within the inclusion at the crests of the long ($C_{v,a}$) and short ($C_{v,b}$) axes are given by

$$C_{v,a} = C_{v,0} \exp[(\Omega(-\gamma_s/r_3 - \sigma_3)/kT]$$

$$C_{v,b} = C_{v,0} \exp[(\Omega(-\gamma_s/r_1 - \sigma_1)/kT] \quad (3)$$

where $C_{v,0}$ is the vacancy concentration in the inclusion at the flat surface under stress free condition at temperature T. Minus signs of interfacial tension and stress terms indicate that the vacancy concentration at the crest decreases with increasing curvature of the crest and comprresional stress. In equation 3, k is the Boltzman's constant and Ω is the volume of one vacancy. Considering $kT \gg |\Omega(-\gamma_s/r_i - \sigma_i)|$, equations 3 are rewritten as

$$C_{v,a} = C_{v,0}[\Omega(-\gamma_s/r_3 - \sigma_3)/kT + 1]$$

$$C_{v,b} = C_{v\,0}[\Omega(-\gamma_s/r_1 - \sigma_1)/kT + 1]. \quad (4)$$

Consequently, the mean gradient of the vacancy concentration between the long and short axes is expressed by

$$grad\ C_v = (C_{v,b} - C_{v,a}) / l$$

$$= -C_{0,v}\Omega\,[\gamma_s\,(1/r_1 - 1/r_3) + (\sigma_1 - \sigma_3)]/kT, \tag{5}$$

in which l is the mean distance between the crests. As l is the length approximately related to $\sqrt{a^2 + b^2}$, we express $l = h\sqrt{a^2 + b^2}$, where h is a constant within the range 1 to $\pi/2\sqrt{2}$. According to Fick's first law, the vacancy flux, J_v, from the long axial crest to the short axial crest becomes

$$\begin{aligned} J_v &= -D_v grad C_v \\ &= \frac{-D_v(C_{v,b} - C_{v,a})}{hkT\sqrt{a^2 + b^2}} \\ &= \frac{C_{v,0}D_v\Omega}{hkT\sqrt{a^2 + b^2}}\left[\gamma_s\left(\frac{1}{r_1} - \frac{1}{r_3}\right) + \left(\sigma_1 - \sigma_3\right)\right] \end{aligned} \tag{6}$$

in which D_v is the diffusion coefficient of vacancies at the boundary of the inclusion and host. The flux of material, J_b, proceeds in the inverse of the flux of vacancy ($J_b = - J_v$).

The flux of material is expressed as

$$
\begin{aligned}
J_b &= \frac{-C_{v,0} D_v \Omega}{hkT\sqrt{a^2 + b^2}} \left[\gamma_s \left(\frac{1}{r_1} - \frac{1}{r_3} \right) + \sigma_1 - \sigma_3 \right] \\
&= \frac{-D_{gb}}{hkTa\sqrt{1 + L^2}} \left[-\gamma_s \left(\frac{a^3 - b^3}{a^2 b^2} \right) + \sigma_1 - \sigma_3 \right] \\
&= \frac{D_{gb}}{hkT\sqrt{1 + L^2}} \left[\gamma_s \left(\frac{1 - L^3}{b^2} \right) - \frac{\sigma_1 - \sigma_3}{a} \right]
\end{aligned}
\tag{7}
$$

in which D_{gb} is the diffusion coefficient for the slowest atom in the interface, using the relation of $D_{gb}=C_{v,0}\Omega D_v$. L is the aspect ratio of inclusion defined as $L = b/a$. The volume increase due to the efflux of the vacancy is obtained as follows:

$$
dV = J_b \Omega S dt, \tag{8}
$$

where S is the total area through which vacancies flow out. In the case of the ellipsoidal inclusion, we have $S=f\pi b\delta$ where δ is the thickness of the interface through which the vacancies flow out, and f is a geometrical constant within the range $\sqrt{3}$ to 2.0 (Fig.1 c). The volume of material transported by boundary diffusion (Fig. 1b) is also expressed as

$$dV = \frac{2V_0}{3\sqrt{3}a}da\,. \tag{9}$$

Considering $dL = d(b/a) = -(3b/2a^2)da$, equation (9) is rewritten as

$$dL = -\frac{9\sqrt{3}L}{4V_0}dV\,. \tag{10}$$

Combining equation (10) with equations (7) and (8), we derive the rate equation for the change of inclusion aspect ratio (dL) as follows:

$$dL = A\frac{D_{gb}\Omega\delta}{R^3kT}\frac{L}{\sqrt{1+L^2}}\left[\frac{(1-L^3)\gamma_s}{RL^{1/3}} - L\sigma\right]dt\,, \tag{11}$$

where A is a constant ($27\sqrt{3}f/16h$), R = grain size ($\sqrt[3]{ab^2}$) and σ = differential stress ($=\sigma_1 - \sigma_3$). Equation (11) illustrates two features characteristic of the change in inclusion shape where two diffusion processes operate. First, the rate of change in aspect ratio depends on the grain size by inverse power law. The rounding component ($\propto \gamma_s$)

depends on R^{-4}, while the diffusion creep component ($\propto\sigma$) depends on R^{-3}. These patterns of size-dependence are consistent with the models published previously by *Toriumi* [1987] and *Coble* [1963], respectively. Second, the inclusion aspect ratio evolves toward a steady state value (*dL=0*). The steady state condition satisfies the relation of

$$\frac{(1-L^3)\gamma_s}{RL^{1/3}} - L\sigma = 0. \qquad (12)$$

Given the interfacial tension γ_s between the inclusion and the host mineral, equation (12) provides the *L-R* patterns under steady state conditions corresponding to the differential stress (Fig. 2). For each steady-state *L-R* pattern, the aspect ratio of the inclusion decreases with increasing grain size. As the differential stress increases, the *L-R* curve shifts to the lower aspect ratio field. It is notable that the *L-R* pattern generated under steady state conditions is not directly related with the absolute values of γ_s and σ, but rather their ratio σ/γ_s.

2-2. Shape development by dislocation creep

[10] *Karato et al.* [1995] proposed the constitutive equation to describe dislocation creep of material crystallized into the garnet structure as

$$d\varepsilon/dt = B(\sigma/\mu)^n \exp(-gT_m/T), \quad (13)$$

where ε is strain, $d\varepsilon/dt$ is strain rate, σ is the differential stress, μ is the shear modulus, T_m is the melting temperature, n is the stress exponent, and B and g are constants, respectively. If we consider the geometry of an inclusion under uniaxial tensile stress (Fig. 1), the increment of strain ($d\varepsilon$) can be converted to the change in the aspect ratio (dL) as follows. The increment of strain is defined as

$$d\varepsilon = da/a. \quad (14)$$

Since $dL = -(3b/2a^2)\,da$, we obtain

$$dL = -(3/2)Ld\varepsilon$$

$$= -(3/2)L\,B(\sigma/\mu)^n \exp(-gT_m/T)dt. \quad (15)$$

The minus sign indicates the elongation of the inclusion. Equation 15 expresses the development of the aspect ratio of the inclusion by dislocation creep. Dislocation creep differs from the diffusion processes in the following ways. First, equation 15 does not relate to grain size, and thus variation in aspect ratio with respect to grain size is not a product of dislocation creep. Second, the differential stress affects the rate of shape change of the inclusion by a power-law relationship. This contrasts with the diffusion creep, for which the stress exponent n is always 1.0.

2-3. Equation governing the shape development of inclusions

[11] Dislocation creep and diffusion processes (diffusion creep, rounding) are not exclusive with each other, but it is considered that all processes are active under differential stress at high temperature. The final expression governing the shape change of the inclusion is written by combining equations 11 and 15 as follows:

$$dL/dt = A\frac{D_{gb}\Omega\delta}{R^3kT}\frac{L}{\sqrt{1+L^2}}\left[\frac{(1-L^3)\gamma_s}{RL^{1/3}} - L\sigma\right] - \frac{3LBexp(-gT_m/T)}{2\mu^n}\sigma^n . \quad (16)$$

3. Application of model to garnet inclusions hosted in quartz

3-1. Sample description

[12] Garnet inclusions in a granulite-facies quartzite from the Skallen district in the Lützow-Holm Complex, East Antarctica, were analyzed to compare with the model results (Fig.3a). The geology and petrology of Skallen are described in *Osanai et al.* [2004]. The metamorphic conditions have been estimated from Skallevikshalsen, adjacent to Skallen, to be 780 – 960 ˚C and 0.6 – 1.1 GPa [*Yoshimura et al.*, 2004]. Temperature over 1000˚C calculated by garnet-orthopyroxene geothermometry has been reported [*Osanai et al.,* 2004], which suggests that these rocks may have undergone the ultra-high temperature metamorphism. The peak metamorphic condition at Skallen remain controversial due to the obscuring effects of retrograde metamorphism [*Ikeda,* 2004]. Petrological studies of metapelites from the Lützow-Holm Complex at Rundvågshetta suggest a P-T trajectory of involving near-isothermal decompression

from peak temperatures higher than 900˚C [*Hiroi et al.*, 1991; *Motoyoshi and Ishikawa,* 1997; *Fraser et al.,* 2000]. The ages of various stages of the metamorphism as estimated by U-Pb zircon age and Ar/Ar data range from ~520 Ma to ~420 Ma. *Fraser et al.* [2000] suggested that rapid exhumation and cooling occurred within a time interval of 20Myr (Fig. 3b).

[13] The sample analyzed in this study is composed of quartz (~ 85 vol/%) and garnet (~ 15 vol/%) with minor secondary minerals including chlorite, plagioclase, mica and opaques (Fig. 4). The mean grain size of quartz is ~5 mm. Grain boundaries of quartz are generally irregular and subgrains are commonly developed with intense undulose extinction. Garnet grains occur as isolated inclusions within the quartz matrix (Fig. 4) and are of homogeneous composition (Prp 22, Alm 68, Grs 8 and Sps 2). A lineation is defined by elongate grains of garnet and a foliation by the occurrence of garnet-rich layers (Fig. 5).

[14] Grain size R ($=(area/\pi)^{1/2}$) and aspect ratio L ($=b/a;\ a>b$) of garnet inclusions were measured in sections cut perpendicular to the foliation and parallel to the lineation (X-Z section). Outlines of garnets were traced from photomicrographs, and shape

parameters were measured using NIH image software. We counted only isolated single garnet grains in quartz grains. In order to exclude polycrystalline aggregates from our measurement, we checked each garnet grain in orientation contrast image (OC-image) by a field emission gun SEM (JEOL JSM6500 in the Center for the Advanced Marine Core Research, Kochi University; *Michibayashi et al.*, [2004]). For OC-images showing grain boundaries, misorientation angles were analyzed by the electron back scattered diffraction techniques (EBSD). Then, only single garnet grains (i.e. garnet inclusions) with low angle grain boundaries were taken into account.

[15] The grain size of garnet inclusions (R) ranges from 10 to 900 μm, with smaller inclusions ($50 < R < 200$ μm) most abundant. The mean grain size is about 100 μm, which is much smaller than that of the matrix quartz grains. Substructures and shape of the garnet inclusions change systematically with increasing grain size. Figure 6 shows OC images and Fig. 7a plots of the aspect ratio (L) – grain size (R) distribution pattern of garnet inclusions. Garnet inclusions of size < 150 μm commonly possess a spherical or ellipsoidal shape (Fig. 6a, b). The aspect ratio of these grains ranges from 0.5 to 1.0 and decreases with increasing grain size (Fig. 7). No substructures are

observed in the small spherical garnet inclusions. Garnet inclusions of size 150 to 300 μm are generally elongate, and are characterized by pinch-and-swell structure. The aspect ratio of these inclusions is commonly smaller than 0.5 (Fig. 7). Although some of these inclusions contain grain or subgrain boundaries at the narrow parts of the pinch-and swell structures (Fig. 6c), most are devoid of substructures (Fig. 6d). Coarse-grained garnets (R > 300 μm) are relatively rare, and show irregular grain boundaries (Fig. 6e), variable aspect ratios and commonly elongate shape. Subgrain boundaries are commonly observed within the coarse-grained garnets (Fig. 6e). The variation in the aspect ratio L (= b/a) of the garnet inclusions with respect to the grain size R is given in Fig. 7a. The mean aspect ratios of garnet inclusions within twelve size ranges are summarized in Table 1 and Fig. 7b. Smaller inclusions (R < 100 μm) are generally sub-spherical (L > 0.7), whereas larger inclusions record smaller aspect ratios (L), with the minimum aspect ratio for the inclusions of size 200 to 250 μm.

[16] To understand 3D shape of garnet inclusions, shape parameters were measured in sections cut perpendicular to both the foliation and the lineation (Y-Z section) and parallel to the foliation (X-Y section). Figure 8 shows a Flinn plot of garnet

inclusions. The lengths of the short axes of inclusions in X-Y section and of the long axis in Y-Z section were compared as the intermediate axis (Y) of 3D shape of inclusions. While smaller grains (Y<400μm) are prolate in shape, larger grains (Y>400μm) are oblate. The point calculated from the mean values of ratios of X/Y and Y/Z is plotted in the prolate region (Flinn coefficient = 1.1).

[17] Crystal preferred orientation (CPO) patterns of the garnet inclusions are shown in Fig. 9. The CPO is presented in the traditional structural frame characterized by the mineral lineation (X) and the foliation normal (Z), with Y being perpendicular to X and Z. The CPO of garnet is quite weak, as it displays pole figure densities as high as 1.69 mean uniform density. Recently, *Mainprice et al.* [2004] presented a result of numerical simulation for pole figures of garnets under dislocation creep. The CPO patterns in Fig.9 have no similarity with those presented by *Mainprice et al.* [2004]. Alternatively, although *Kleinschodt and McGrew* [2000] compare the maxima of (111), (110) and (100) poles of measured CPO with positions of axes of garnet single crystal with <111> parallel X and (110) in X-Y, there is no similarity between the CPO patterns in Fig.9 and positions of axes of garnet single crystal. As a consequence, we have found

no means of interpreting the CPO of garnet in our sample.

3.2 Values of parameters used in the calculation

[18] In the following section, the shape development of garnet inclusions within quartz is investigated following equation 16. Values of parameters used in the calculations are listed in Table 1. The value of parameter A in equation 16 ranges 4.54 ($h = \pi/2\sqrt{2}$, $f = \sqrt{3}$ at $L = 1.0$) to 5.84 ($h = 1.0$, f =2.0 at $L = 0$). In the calculation, the value of A is set to be 5.0, assuming the geometrical parameters of $h = 1.1$ and $f = 1.9$. We assume a constant temperature of 950˚C during the shape development of the inclusion, following *Yoshimura et al.* [2004]. According to *Fraser et al.* [2000], the duration at high temperature of > 900˚C is about 10 Myr, which corresponds to the near-isothermal decompression. We assume that the upper limit of the duration of the shape development of garnet is 20 Myr. The initial aspect ratio of the inclusion is assumed to be 1.0, which may be suitable for isotropic minerals such as garnet.

[19] The magnitude of interfacial tension between mineral pairs has been measured in previous studies. *Hiraga et al.* [2002] calculated the interfacial energies for the

boundaries of quartz/quartz, albite/albite, and quartz/albite of 270±110, 300±150, and 250±120 (mJ/m^2; $\times 10^{-3}$ N/m), respectively. The grain boundary energy of olivine has been estimated to be 900±350 mJ/m^2 [*Cooper and Kohdlstedt*, 1982], and ~ 1400 mJ/m^2 [*Duyster and Stöckhert*, 2001]. Thus, interfacial energies between silicates are expected to range 100 ~ 2000 (mJ/m^2; $\times 10^{-3}$ N/m). The interfacial energy of the garnet / quartz boundary (γ_{grtqtz}) can be estimated using the published data of the interfacial energy of quartz/quartz boundary and the dihedral angle (θ) at the quartz-garnet-quartz triple junction from the relation of $\gamma_{grtqtz} = \gamma_{qtzqtz} / 2\cos(\theta/2)$. Using γ_{qtzqtz} = 270±110 (mJ/m^2) [*Hiraga et al.*, 2002] and θ = 133°[*Vernon*, 1968], we obtain γ_{grtqtz} = 340±140 (mJ/m^2). However, it should be noted that the interfacial energy at the quartz / quartz boundary was estimated under wet conditions [*Hiraga et al.*, 2002]. The sample from East Antarctica is considered to have been dry at the high temperatures. Thus, the magnitude of γ_{grtqtz} estimated above would be a minimum, and we set the magnitude of γ_{grtqtz} to be 1000 mJ/m^2 (= 1.0 N/m) in the following calculations. Values of constants (*B*, *g*) and the stress exponent (*n*) in the constitutive equation for garnet (eq. 13) are as determined by *Karato et al.* [1995]. The values of shear modulus (μ) and melting

temperature (T_m) vary with the composition of garnet. We used the data of μ and T_m for the specimen "alm-pyro" in *Karato et al.* [1995], because its chemical composition (Alm68, Prp20, Grs12) is close to that of our sample.

[20] There are limited data for the value of the interface diffusion coefficient (D_{gb}) and boundary-width (δ) between garnet and quartz. Following *Joesten* [1991], we assume the boundary-width to be 1.0 nm. In general, the diffusion coefficient of oxygen is much smaller than that of cations in silicates [*Joesten,* 1991]. Thus, the slowest atom may be oxygen at the garnet/quartz boundary. Although we do not have the value of the interface diffusion coefficient of oxygen of garnet-quartz boundary, there are several experimental data of lattice or grain boundary diffusion of oxygen in silicates. Since diffusion is a thermally-activated process, the magnitude of diffusion coefficient varies with increasing temperature. Diffusion coefficients of various minerals are conventionally compared against normalized temperatures (T_m/T). Considering the temperature of 950 ˚C, the value of T_m/T is 1.34 for garnet. The grain-boundary diffusion coefficient is generally 10^4~10^5 times higher than volume diffusion coefficient. In the case of forsterite, $D_{oxygen}^{GB}/ D_{oxygen}^{VOL}$ attains 10^5~10^8 [*Joesten*, 1991]. The

volume diffusion coefficients of oxygen in grossular ($Ca_3Al_2Si_3O_{12}$) and YIG ($Y_3Fe_5O_{12}$) are ~ 1.0×10^{-20} and ~ 1.0×10^{-15} m^2/s at T_m/T of 1.3~1.4 [*Chakraborty and Ganguly*, 1992; *Paladino et al*., 1964; *Karato et al*., 1995]. In this study, we investigate the value of D_{gb} ranging 1.0×10^{-10} ~ 1.0×10^{-14} m^2/s.

3.3 Model results

[21] If inclusions deform only by dislocation creep, variation in the aspect ratio with respect to grain size does not occur. Figure 10 shows the progressive evolution of aspect ratio by dislocation creep following equation 15. The relation between the rate of shape change of an garnet inclusion and differential stress is comparable to that between strain rate and differential stress. Strain rates are calculated with given differential stresses, respectively (Table 3). As the magnitude of differential stress increases from 0.1 to 1.2, the strain rate increases markedly from 5.85×10^{-17} to 4.80×10^{-14} s^{-1}. As seen in Fig. 10, the effect of dislocation creep on the shape change of a garnet inclusion is negligible small in the case of $\sigma < 0.1$ MPa

[22] The progressive evolution of the aspect ratio (L) of the inclusions is calculated

following equation 16. Figure 11 shows results for σ = 0.1 MPa and $D_{gb} = 1.0\times10^{-12}$ m^2/s. Values of other parameters are listed in Table 2. The aspect ratio of small grains (R = 5, 10. 20. 40, 60 μm) changes rapidly and reaches a steady state value ($dL/dt = 0$) within 5 Myr. For each grain size, the rate of change in the aspect ratio decreases, as the aspect ratio approaches the steady state value. The value of the steady state aspect ratio decreases with increasing grain size and/or increasing differential stress. This trend is similar to that of diffusion-only processes (Fig. 9), but the absolute value of the steady state aspect ratio is somewhat smaller because of the dislocation creep component. Coarse grains (R = 100, 200, 300, 400, 600 μm) have not yet reached steady state at t = 20 Myr. The time taken for the inclusion aspect ratio to achieve a steady state drastically increases with increasing grain size.

[23] The progressive evolution of the L-R distribution pattern of garnet inclusions is tested for fifteen cases with various magnitudes of the diffusion coefficient and the differential stress: $D_{gb} = 1.0\times10^{-10}$, 1.0×10^{-11}, 1.0×10^{-12}, 1.0×10^{-13}, 1.0×10^{-14} m^2/s and σ = 0.01, 0.1, 1.0 MPa (Fig. 12). It is apparent that all L-R patterns have the minimal aspect ratio for the intermediate grain size. The grain size with the minimum

aspect ratio (R_{Lmin}) is nearly equal to the maximal grain size of the inclusions, which achieve a steady state aspect ratio. The coarser grains ($R > R_{Lmin}$) have not yet reached at a steady-state aspect ratio. The magnitude of R_{Lmin} shifts to the larger value as time advances. The size-dependency of the *L-R* evolution patterns is due to the diffusion processes (first term of eq. 16), and this is confirmed by the fact that R_{Lmin} is larger with an increase in the diffusion coefficient. The *L-R* patterns dominated by diffusion processes are predominant where $\sigma = 0.01$ MPa (Fig. 12 a, b, c, d, e), because the effect of dislocation creep is negligible under low stress conditions (Fig. 10). The effect of dislocation creep is evident from the decrease of aspect ratio, which is independent of grain size. The evolution of the *L-R* pattern dominated by dislocation creep is observed for coarser grains especially in the case of the smaller value of the diffusion coefficient, and of the larger differential stress (Fig. 11 j, m, n, o). As the differential stress affects the strain rate by a power-law relationship ($n = 2.7$) in the dislocation creep, the rate change in inclusion shape rapidly increases with increasing differential stress.

3.4 Comparison of theoretical L-R curve with measured L-R pattern of garnet inclusion

from Skallen: Estimates of duration and differential stress for shape development

[24] The observed *L-R* pattern of garnet inclusions from Skallen can be compared with the model results, because the sample shows the features comparable to the assumptions of the model; (1) garnets occur as isolated mineral inclusions (Fig. 4), (2) garnets commonly have a curved outline and prolate shape, which is approximated to be a rotational ellipsoid (Fig. 4, 6, 7), and (3) the symmetry of garnet shapes indicates the coaxial deformation. Constrictional coaxial strain is expected from the prolate shape of inclusions and well-developed lineation. In the following, we attempt to estimate the magnitude of differential stress and the duration of the shape development of garnet inclusions, by comparing the theoretical *L-R* curve with the observed *L-R* pattern. If a value of diffusion coefficient is given, the aspect ratio of the inclusion with each grain size is calculated as a function of time and differential stress. The observed aspect ratio data for the twelve grain sizes are summarized in Table 1. We calculate the residuals of the aspect ratio defined as $L_i^{calc} - L_i^{obs}$, where L_i^{calc} and L_i^{obs} are the calculated aspect ratio and observed mean aspect ratio for the i th grain size, respectively. The optimal values of σ and t are calculated by the simple least squares method to minimize the sum

of the residuals,

$$\Delta L^2 = \frac{1}{12}\sum_{i=1}^{12}(L_i^{calc} - L_i^{obs})^2 \quad . \tag{17}$$

In the regression, we evaluate the ΔL^2 value for the ranges of t = 0~20 Myr (0.1 Myr step) and σ = 0~2.0 MPa (0.001 MPa step).

[25] Best-fitted conditions were evaluated for five cases with $D_{gb} = 1.0\times10^{-10}$, 1.0×10^{-11}, 1.0×10^{-12}, 1.0×10^{-13}, 1.0×10^{-14} m^2/s, respectively (Table 4, Fig. 13). For each case, we found two local minimums of ΔL^2 in the t – σ space: (1) high stress and short time condition (σ > 1.0 MPa, t < 1.0 Myr) and (2) low stress and long time condition (σ < 0.1 MPa, t > 10 Myr). Which condition yields the real minimal ΔL^2 value varies with the value of diffusion coefficient. In the cases with higher diffusion coefficient (conditions 1, 2, 3), the minimal ΔL^2 value is found in the low stress condition (Table 4, Fig. 13), whereas in the cases with lower diffusion coefficient (conditions 4, 5) it is found in the high stress condition (Table 4, Fig. 13). Local minimums of ΔL^2 are produced due to the contradictory L-R patterns between coarser grains (R > 250μm) and

finer grains (R < 250μm). The L-R pattern of garnet inclusions < 250 μm is fitted to the theoretical L-R pattern of low stress condition (curves 1, 2, 3 in Fig. 13). The best-fitted condition is σ = 0.014 MPa and t = 13.8 Myr with $D_{gb} = 1.0 \times 10^{-10}$ m^2/s (condition 1 in Table 1, Fig. 13). In this condition, diffusion processes (diffusion creep, rounding) are dominant. On the other hand, the L-R distribution of coarse grains (R > 250μm) deviates from theoretical curves under such a low differential stress. The observed L-R pattern of coarse grains (R > 250μm) having a constant aspect ratio is better explained by high stress conditions, that favors dislocation creep (Fig. 13 curves 4, 5). However, in high stress conditions, the calculated L-R pattern of fine grains is quite different from the observed pattern. The optimal values of conditions 4 and 5 (t = 1.0 Myr) partly result from artificial effect of the calculation step (0.1 Myr step) and of the upper limit of differential stress (2.0 MPa) (Table 4). From dislocation-creep-dominant L-R pattern, we cannot estimate a single solution of σ and t, respectively, because of the lack of the size dependency of aspect ratio. If one of σ and t is given, the other is determined.

[26] The minimal ΔL^2 value among all cases is found in the condition 1 (Table 4, Fig. 13). Even for this condition, however, there is a discrepancy between the observed

and theoretical *L-R* patterns for the coarse grains (Fig. 13). The contradictory *L-R* patterns between coarser and finer grains indicate that a single stage of differential stress cannot explain the *L-R* pattern of all garnet inclusions.

[27] To explain both segments of the observed *L-R* pattern (fine-grained and coarse-grained regions), it is better to consider at least two stages with different stress conditions. Here we consider a case of two-stage episode: high stress condition (stage A) and low stress condition (stage B). At stage A ($t = 0 \sim t_A$), inclusions are stressed by the differential stress of σ_A, and after that, they are stressed by σ_B at the stage B ($t = t_A \sim t_B$) (Fig. 14a). The magnitude of diffusion coefficient at each stage is assumed to be $D_{gb,A} = 1.0 \times 10^{-11}$ m_2/s and $D_{gb,B} = 1.0 \times 10^{-12}$ m^2/s, respectively. In this two-stage case, the *L-R* curve is determined by four parameters, σ_A, σ_B and t_A, t_B. Assuming $\sigma_A = 1.0$ MPa, we found values of three parameters to minimize the value of ΔL^2 given in eq. 17. The best fitted solutions for σ_B, t_A and t_B were obtained to be 0.014 MPa, 0.5 Myr and 14.4 Myr, respectively (Fig. 14b, c). For this condition, the value of ΔL^2 is 0.000600, which is much smaller than that of cases of a single-stage.

[28] It should be noted that we cannot determine the magnitude of differential

stress at the high-stress stage (σ_A), at which dislocation creep is dominant. The information of this stage is recorded only in the *L-R* pattern of the coarse grains (>250 μm), because the *L-R* pattern of fine grains were completely modified at the low-stress stage (stage B). Under the dislocation creep dominant regime (Fig. 14b, $R > 250\mu m$), the size dependency of aspect ratio of inclusion is small. Therefore, the relation between t_A and σ_A is trade-off, and we cannot determine both t_A and σ_A simultaneously from the *L-R* distribution pattern. If the magnitude of σ_A increases, the duration at stage A (t_A) is shorter. This is the reason for assuming σ_A in the above calculation. However, the uncertainties in σ_A does not affect on the estimates of σ_B and t_B, as long as $\sigma_A > 0.5$ MPa. In the case of $\sigma_A < 0.5$ MPa, the duration of stage A (t_A) becomes longer, and thus the *L-R* pattern of coarse grains must be more curved due to the effect of diffusion processes. Since the garnet inclusions show relatively constant aspect ratio in coarse-grain region, differential stress is expected to be larger than 0.5 MPa at stage A.

[29] At stage B, the aspect ratio (L) of finer grains rapidly increases toward a steady state condition of $\sigma = 0.014$ MPa, while the aspect ratio of coarser grains slightly decreases (Fig. 14c). This indicates that the rounding process selectively operates on

fine grains. The result of this two-stage situation is well consistent with the observed *L-R* patterns of garnet inclusions (Fig. 14c, t_B = 14.4Myr).

4. Discussion

4.1 Comparison with other models

[30] The diffusion creep component of the rate of change in aspect ratio of an inclusion is converted to the strain rate as follows:

$$d\varepsilon/dt = A' \frac{D_{gb}\Omega\delta}{R^3 kT} \frac{L^2\sigma}{\sqrt{1+L^2}} \quad , \tag{18}$$

where $A' = 2/3\ A = 9\sqrt{3}f / 8h$. The part of $D_{gb}\Omega\delta\sigma/R^3kT$ is completely consistent with that in the constitute equation of diffusion creep given by *Coble* [1963]. A difference between the present model and the model of *Coble* [1963] is the assumption in terms of the shape of a grain. *Coble* [1963] assumes a spherical grain with a constant aspect ratio of 1.0, whereas we assume a rotational ellipsoidal grain with changeable aspect ratio. As a result, the characteristic distance of diffusion, *l,* changes with varying aspect ratio.

Considering the geometry of a sphere [*Coble*, 1963], the length between pole and equator is $\pi R/2$. The length depends on the aspect ratio for rotational ellipsoid as $l \approx h\sqrt{a^2 + b^2} = ha\sqrt{1 + L^2}$, where h is a constant (Fig. 1a). As a result, the strain rate of an inclusion varies with the aspect ratio under the same differential stress in our model.

[31] *Ford and Wheeler* [2004] presented an interface diffusion creep model in two-phase polycrystalline materials. They treated the flux of material along the interface as being the proportional to the chemical potential gradient as

$$J = - D_{os} \partial\mu/\partial x, \tag{19}$$

where D_{os} is the Onsager diffusion coefficient and μ is chemical potential. The fundamental equation linking stress and chemical potential along an interface is

$$\mu = \overline{F} + \overline{V}\sigma_n, \tag{20}$$

where $\overline{F}$ and $\overline{V}$ are the Helmholtz free energy and molar specific volume of the grain

adjacent to the interface, and σ_n is the normal component of stress across the interface (compressional stress is positive) respectively. *Ford and Wheeler* [2004] assume the variation in $\overline{F}$ is negligible so that chemical potential is a linear function of normal stress. When we consider the curvature of the surface, equation 20 is modified to

$$\mu = \overline{F} + \overline{V}\sigma_n + 2\gamma_s / r, \tag{21}$$

where r is the local radius of curvature (assuming a spherical cap geometry) and γ_s is the interfacial tension. Suppose we regard the grain boundary as being an "ideal solution" of a solid species, then

$$\mu = \mu_0 + RT\, lnC, \tag{22}$$

where C is concentration of a solid species and μ_0 is chemical potential at a standard state. With an appropriate reference state for C_0, we get

$$C = C_0 \exp [(\sigma_n \overline{V} + 2\gamma_s / r)/RT]. \quad (23)$$

If we assume that vacancies are in equilibrium with the solid surface, then

$$C_v = C_{v,0} \exp [(-\sigma_n \overline{V} - 2\gamma_s /r)/RT]. \quad (24)$$

This equation is very similar to equation 3 that relates to vacancies. Therefore, in spite of the difference in the introduction of flux of material, the present model is comparable to the model with chemical potential as shown in *Ford and Wheeler* [2004]. *Ford and Wheeler* [2004] consider the interface network associated with phases A and B, and three types of interfaces are considered: A/A, A/B, B/B. The chemical currents for phase A and B are defined independently. In contrast, the inclusion-host system analyzed in this study has only the garnet / quartz interface, so that there must be some interaction between quartz dissolving and garnet precipitating (or vice versa). One expects the rates to be equal so that we do not open up gaps. But Ford and Wheeler would predict a "space problem" even in this simple geometry. This is because in general a net

convergence or divergence of grains is predicted at A/B-type interface (e.g. eq. 14 of *Ford and Wheeler*, 2004). One way round this would be to hypothesize that at these high temperatures quartz was quite soft, due to easy dislocation creep. This additional deformation mechanism might assist in "closing the gaps", and it may be appropriate to consider the diffusive flux of the slowest atom at the interface.

4.2 Deformation mechanism of garnet at high temperature

[32] A number of studies have reported plastically deformed garnet from granulite, eclogite and garnet-peridotite rocks [*Ando et al*., 1993; *Ji and Martignole*; 1994, *Kleinschrodt and McGrew*, 2000; *Kleinschrodt and Duyster*, 2002; *Ji et al*., 2003; *Terry and Heidelbach*, 2004]. Most of these studies suggested that dislocation creep is the dominant deformation mechanism for garnet, based on observations of dislocation network and subgrain wall by TEM, or analyses of crystal orientation pattern (CPO) [*e.g. Ji and Martignole*, 1994; *Kleinschrodt and McGrew*, 2000; *Kleinschrodt and Duyster*, 2002*; Mainprice et al*., 2004]. Several experimental studies have also suggested that silicate garnet deforms at high temperatures by dislocation creep [*Karato*

et al., 1995; *Voegle et al*., 1998]. The elongate shape and pinch-and-swell structure of garnet analyzed in this study are similar to those reported by *Ji and Martignole* [1994], *Kleinschrodt and McGrew* [2000] and *Kleinschrodt and Duyster* [2002]. *Kleinschrodt and Duyster* [2002] classified garnets in the granulite-facies rocks into three groups: large garnets, numerous elongate garnets, and very small garnet with subspherical shape. Their observation that the most elongate garnets are of intermediate size is consistent with the *L-R* pattern in our sample. *Kleinschrodt and Duyster* [2002] interpreted the subspherical shape of fine-grained garnets as the result of being pinched off from the elongate garnets. Such boudinage process would be possible, but the systematics of the *L-R* pattern in our sample indicates the effect of the rounding process during the annealing stage. In contrast with the results of *Kleinschrodt and McGrew* [2000] and *Kleinschrodt and Duyster* [2002], garnets from Skallen show very weak CPO patterns. In our sample, subgrains are observed in coarse-grained garnet ($R > 300\mu m$), but are not observed in small grains. There seems no correlation between the development of subgrains and the elongation of garnet inclusions. Accordingly, it is difficult to determine the deformation mechanism solely from the CPO analysis and the

observation of substructures. On the other hand, the *L*-*R* pattern analysis presented in this paper suggests that dislocation creep was necessary to explain the elongation of coarser grains ($R > 200\mu m$) within the geological time scale.

[33] Dislocation creep and diffusion creep are considered to be deformation mechanisms affecting crustal rocks at high temperatures, and which of these is dominant is a controversial topic. Although previous studies indicate that dislocation creep is active in the deformation of garnet, few consider how extent diffusion creep contributes to the deformation. The effect of diffusion creep is only revealed from its size dependence. The *L*-*R* distribution pattern provides an insight as to which mechanism is dominant. To consider the various contributions of dislocation creep, diffusion creep and rounding, it is convenient to evaluate the magnitude of each component in the rate of the change in the aspect ratio of garnet inclusions with various grain sizes (diffusion creep: dL_{dfc}/dt, dislocation creep: dL_{dsc}/dt, rounding: dL_{rd}/dt). The values of dL_{dfc}/dt and dL_{dsc}/dt are negative and the total rate of the change in the aspect ratio is written by their summation as $dL/dt = dL_{dfc}/dt + dL_{dsc}/dt + dL_{rd}/dt$ (eq. 16). For example, we consider the deformation history corresponding to the two-stage

deformation shown in Fig. 14. Figure 15a, b, and c correspond to the high stress stage (stage A; 1.0 MPa) and d, e, and f to subsequent low stress stage (stage B; 0.014 MPa). At $t = 0$, the component of rounding is zero, because the initial aspect ratio of inclusions is 1.0 (Fig. 14a). Despite the fact that dislocation creep is independent of grain size, $-dL_{dsc}/dt$ varies with respect to grain size in Fig. 14b and c. This is because the magnitude of $-dL_{dsc}/dt$ is affected by the aspect ratio L (eq. 15). The curved lines of $-dL_{dsc}/dt$ reflect the variation in the aspect ratio with respect to grain size at $t = 0.1$ and 0.4 Myr (Fig. 14b, c). At stage A, curves of diffusion creep and dislocation creep cross around the size of 300 μm, which indicates a shift in the dominant deformation mechanism (Fig. 15a, b, c). Diffusion creep is dominant in the fine-grain region, and dislocation creep is dominant in the coarse-grain region. The magnitude of $-dL_{dsc}/dt$ at stage B is much smaller than that at stage A, reflecting lower differential stress. The magnitude of $-dL_{dsc}/dt$ ranges from 2.0×10^{-13} ~2.0×10^{-9} year^{-1}, which is always smaller than the magnitude of $-dL_{dfc}/dt$ for grain sizes of 0~600 μm. Therefore, diffusion creep is always dominant at stage B. The curves of $-dL_{dfc}/dt$ and $-dL_{rd}/dt$ cross around 250 μm at stage B (Fig. 15d, e, f). Which is dominant between diffusion creep and

rounding is determined by values of the aspect ratio at the instance. At t = 10.5Myr, the curves of $-dL_{dfc}/dt$ and $-dL_{rd}/dt$ are similar with each other, especially for the region of R < 250 μm (Fig. 15f). This indicates that the aspect ratio of garnet has nearly achieved at the steady-state value. In summary, the results shown in Fig. 15 indicates that (1) both dislocation creep and diffusion creep can be dominant mechanism under the same physical conditions if a variation in grain size exists, and (2) the critical grain size of the transition of the deformation mechanism is determined by the magnitudes of interface diffusion coefficient and differential stress.

4.3 Importance of the low-stress stage for grain shape development

[34] The observed *L-R* pattern of garnet inclusions from Skallen is best explained by a two-stage history of high stress condition subsequent to low stress condition (Fig. 14). For small grains of R < 250μm, the aspect ratios reached at steady-state value at the condition of $\sigma_B = 1.4 \times 10^{-2}$ MPa. Since the contribution of dislocation creep is negligible at the stage B (Fig. 15 d, e, f), the magnitude of the differential stress at a steady state relates to the magnitude of the interfacial tension at garnet/quartz boundary

(Fig. 9). In spite of uncertainty in the magnitude of the interfacial tension, the estimated value would not change by more than one order. Therefore, the magnitude of differential stress at the stage B is expected to be much smaller than that of the lower crust (10 ~ 200 MPa) estimated in previous studies [*e.g. Ranalli*, 1984; *Michibayashi,* 1993]. The small magnitude of the differential stress is consistent with the large grain size of matrix quartz (>5mm) in the analyzed sample. The stage B may be the period of static annealing after intense deformation. Subgrain boundaries observed in the coarse garnet grains would have been formed by rearrangement of dislocation during this stage (Fig. 6c, e). It is interesting that the magnitude of σ_B is non-zero. Very small differential stress can affect the shape of inclusions, because the interfacial tension between the silicates (~1.0 N/m) is much smaller than tectonic stress.

[35] Within the analyzed sample, most elongated garnet inclusions are found in the size range at R = 200~250 μm (Fig. 5). This critical grain size provides an important constraint on the interface-diffusion coefficient, because the size of grains with minimum aspect ratio indicates the characteristic length that were affected by diffusion processes during the period of deformation. As the magnitude of the diffusion

coefficient decreases, the characteristic length becomes smaller (Fig. 12). Considering the duration of < 20 Myr, the value of D_{gb} is required to be larger than $1.0 \times 10^{-11} m^2 s^{-1}$ at stage B. We found that the annealing time ($t_B - t_A$ = 13.7 Myr) is ten times greater than the deformation time (t_A = 0.5 Myr). This may indicate that high stress conditions within the lower crust are only short periods of geological time.

4.4 Wider significance

[36] The model outlined in this study describes dislocation creep and interface diffusion in response to both interfacial tension and differential stress. Although we consider a uniaxial extension for simplicity, the shape of coarse-grained garnet inclusion deviates from a rotational ellipsoid (Fig. 8). Thus, further development of the model will be required to constrain physical conditions more accurately. The model is easily amended to describe other types of coaxial deformation relevant to the deformation of rocks under stress at high temperatures. The elongate shape of garnet described here may not be particularly common, because garnet generally is less deformed than other silicates during metamorphism. However, the analysis of the *L-R* pattern of mineral

inclusions presented in this study is potentially applicable to various types of metamorphic, magmatic and mantle rocks, because mineral inclusions are common in these rocks. There have been several descriptions of the rounding of mineral inclusions, including quartz inclusion in albite [*Toriumi,* 1987], and spinel and olivine inclusions within orthopyroxene in peridotite [*Toriumi,* 1981]. The physical processes modeled here would generally proceed under stress at high temperatures. Thus, the analysis of the *L-R* pattern will provide us the insights of the contributions of dislocation creep, diffusion creep and rounding processes. Furthermore, improved quantitative estimates of several material parameters such as the interfacial tension, interface diffusion coefficient, and of parameters incorporated in the constitutive equation will allow us to further constrain the magnitude of differential stress and duration deduced from the *L-R* distribution pattern.

[37] Acknowledgements. M. Toriumi and T. Masuda are acknowledged for their constructive comments and encouragements. We greatly thank T. Masuzawa for encouragement and T. Ikeda and T. Kawakami for providing the sample. A. Stallard is gratefully acknowledged for improving the early version of the manuscript. We are also

grateful to T. Hiraga and Y. Takei for their discussion. The critical and constructive reviews by J. Wheeler and S. Ji improved the paper significantly. This work was partially supported by a JSPS research fellowship (200300476).

References

Ando, J., K. Fujino, and T. Takeshita (1993), Dislocation microstructures in naturally deformed silicate garnets. *Physics of the Earth and Planetary Interiors, 80*, 105-116.

Chakraborty, S., and J. Ganguly (1992), Cation diffusion in aluminosilicate garnet: experimental determination in spessartine-almandine diffusion couples, evaluation of effective binary diffusion coefficients, and applications. *Contrib. Mineral. Petrol., 111*, 74-86.

Coble, R. L. (1963), A model for Boundary Diffusion Controlled Creep in Polycrystalline Materials. *J. Appl. Phys., 34,* 1679-1682.

Cooper, R. F., and D. L. Kohlstedt (1982), Interfacial energies in the olivine-basalt system, in *High-pressure research in geophysics, Adv. Earth. Planet. Sci. 12*, edited by S. Akimoto and M. H. Manghnami, pp. 217-228, Center for Academic Publications Japan, Tokyo.

Duyster, J., and B. Stöckhert (2001), Grain boundary energies in olivine derived from microstructures. *Contrib. Mineral. Petrol., 140*, 567-576.

Ford, J. M., and J. Wheeler (2004), Modelling interface diffusion creep in two-phase

materials. *Acta Materialia*, 52, 2365-2376.

Fraser, G., D. J. McDoucgall, D. J. Ellis, and I. S. Williams (2000), Timing and rate of isothermal decompression in Pan-African granulites from Rundvågshetta, East Antarctica. *J. Metamorphic Geol., 18*, 441-454.

Herring, C. (1950), Diffusional viscosity of a polycrystalline solid. *J. Apply. Phys., 21*, 437- 445.

Hiraga, T., O. Nishikawa, T. Nagase, M. Akizuki, and D. L. Kohlstedt (2002), Interfacial energies for quartz and albite in pelitic schist. *Contrib. Mineral. Petrol., 143*, 664-672.

Hiroi, Y., K. Shiraishi, and Y. Motoyoshi (1991), Late Proterozoic paired metamorphic complexes in East Antarctica, with special reference to the tectonic significance of ultramafic rocks, in *Geological Evolution of Antarctica*, edited by M. R. A. Thomson et al., pp. 83-87, Cambridge Univ. Press, Cambridge.

Ikeda, T. (2004), Garnet-biotite geothermometry of a pelitic gneiss from the Lützow-Holm Complex in Skallen, East Antarctica: Constraints on retrograde metamorphism. Polar Geosci., 17, 45-56.

Ji, S., and J. Martignole (1994), Ductility of garnet as an indicator of extremely high temperature deformation. *J. Structural Geol., 16*, 985-996.

Ji, S., K. Saruwatari, D. Mainprice, R. Wirth, Z. Xu, and B. Xia (2003), Microstructures, petrofabrics and seismic properties of ultra high-pressure eclogites from Sulu region, China: implications for rheology of subducted continental crust and origin of mantle reflections. *Tectonophysics, 370*, 49-76.

Joesten, R. (1991), Grain-boundary diffusion kinetics in silicate and oxide minerals, in *Diffusion, atomic ordering, mass transport: selected topics in geochemistry, Advances in Physical Geochemistry, vol.8* edited by J. Ganguly, pp. 345-395, Springer Verlag, New York.

Karato, S., Z. Wang, B. Liu, and K. Fujino (1995), Plastic deformation of garnets: systematics and implications for the rheology of the mantle transition zone. *Earth Planet. Sci. Lett., 130*, 13-30.

Kingery, W. D., H. K. Bowen, and D. R. Uhlmann (1976), *Introduction to Ceramics*, 2nd ed., p. 1032, A Wiley-Interscience, New York.

Kleinschrodt, R., and A. McGrew (2000), Garnet plasticity in the lower continental

crust: implication for deformation mechanisms based on microstructures and SEM-electron channeling pattern analysis. *J. Structural Geol., 22*, 795-809.

Kleinschrodt, R., and J. P. Duyster (2002), HT-deformation of garnet: an EBSD study on granulites from Sri Lanka, India and the Ivrea Zone. *J. Structural Geol., 24*, 1829-1844.

Mainprice, D., J. Bascou, P.Cordier, and A. Tommasi (2004), Crystal preferred orientations of garnet: comparison between numerical simulations and electron back-scattered diffraction (EBSD) measurements in naturally deformed eclogites. *J. Structural Geol.*, 26, 2089-2102.

Michibayashi, K. (1993), Syntectonic development of a strain-independent steady-state grain size during mylonitization. *Tectonophysics, 222*, 151-164.

Michibayashi, K., A. Okamoto, T. Masuzawa, T. Kawakami, T. Ikeda, and H. Yasuda (2004), Orientation contrast images of garnet in granulite-facies quartzite, Lützow-Holm Complex, East Antarctica. *J. Geol. Soc. Japan, 110*, V-VI.

Motoyoshi, Y., and M. Ishikawa (1997), Metamorphic and structural evolution of granulites from Rundvågshetta, Lützow-Holm Bay, East Antarctica. The Antarctic

Region: Geological Evolution and Processes, ed. by C. A. Ricco. Siena, *Terra Abstract, Publ*., 65-72.

Nabarro, F. R. N. (1948), Deformation of crystals by the motion of single ions. *Report of a Conference on Strength of Solids (Bristol). The Physical Soc.*, 75-90.

Osanai, Y., T. Toyoshima, T. Tsunogae, T. Hokada, W. Crowe, T. Ikeda, T. Kawakami, Y. Kawano, T. Kawasaki, M. Ishikawa, Y. Motoyoshi, and K. Shiraishi (2004), Geological map of Skallen, Antarctica (Revised Edition). Abstract. Map. Ser., Sheet 39 (with explanatory text 23 p.). Tokyo, Natl. Inst. Polar Res..

Paladino, A. E., E. A. Maguire, and L. G. Rubin (1964), Oxygen ion diffusion in single-crystal and polycrystalline yttrium ion garnet. *J. Am. Ceram. Soc*., 47, 280-282.

Poirier, J. P. (1985), *Creep of crystals: High-temperature deformation process in metals, ceramics and minerals*, pp. 260, Cambridge Univ. Press, Cambridge.

Ranalli, G. (1984), Grain size distribution and flow stress in tectonites. *J. Structural Geol. 6*, 443-447.

Rast, N. (1965), Nucleation and growth of metamorphic minerals, In *Controls of Metamorphism,* edited by W. S. Pitcher and G. S. Flinn, pp. 73-102, Oliver and Boyd,

Edinburgh.

Shewmon, P. G. (1963), *Diffusion in solids*, 203 pp., McGraw-Hill, New York.

Spry. A. (1969), *Metamorphic Textures*, 352 pp., Pergamon, Oxford.

Terry, M. P., and F. Heidelbach (2004), Superplasticity in garnet from eclogite facies shear zones in the Haram Gabbro, Haramsoya, Norway. *Geology*, 32 281-284.

Toriumi, M. (1979), A mechanism of shape-transformation of quartz inclusions in albite of regional metamorphic rocks. *Lithos, 12,* 325-333.

Toriumi, M. (1987), Progressive deformation and annealing of quartz inclusion in porphyroblastic feldspar during synmetamorphic non-coaxial deformation. *J. Japan. Assoc. Min. Petr. Econ. Geol., 82,* 123-131.

Toriumi, M. (1981), Rounded mineral inclusions in upper mantle peridotite. *Physics of the Earth and Planetary Interiors*, 27, 39-46.

Yoshimura, Y., Y. Motoyoshi, T. Miyamoto, E. Grew, C. J. Carson, and D. J. Dunkley (2004), High-grade metamorphic rocks from Skallevikshalsen in the Lützow-Holm Complex, East Antarctica: Metamorphic conditions and possibility of partial melting. *Polar Geosci.*, 17, 57-87.

Vernon, R. H. (1968), Microstructures of high-grade metamorphic rocks at Broken Hill, Australia. *J. Petrol., 9*, 1-22.

Voègele, V., J., I., Ando, P., Cordier, R. C. Liebermann (1998) Plastic deformation of silicate garnets I. High-pressure experiments, *Physics of the Earth and Planetary Interiors, 108,* 305-318.

Figure captions

Fig. 1 (a) Ellipsoidal inclusion (ellipsoid axis $a>b$) under stress of $\sigma_1 = \sigma_2 > \sigma_3$. (b) Shape of inclusion after time dt. The shaded area represents the volume of material transported by interface diffusion (dV). (c) The area through which vacancies flow out (S). δ and f indicate grain boundary width and geometrical constant.

Fig. 2 Theoretical curves of the aspect ratio (L) – grain size (R) distribution pattern at the steady state ($dL=0$), when diffusion processes are considered. Seven curves are shown for different values of σ/γ_s.

Fig. 3 (a) Locality of Skallen in East Antarctica, and (b) metamorphic P-T conditions of Skallevikshalsen [*Yoshimura et al.,* 2004] and Rundvågshetta [*Motoyoshi and Ishikawa,* 1997], and *P-T-t* path of Lützow-Holm Complex proposed by *Fraser et al.* [2000].

Fig. 4 Microphotograph of the granulite facies quartzite analyzed in this study (crossed

polar). Black grains are garnet inclusions, and light gray parts are quartz matrix. (a) Section cut perpendicular to foliation and parallel to lineation (X-Z section), and (b) section parallel to foliation (X-Y section). Scale bars indicate 1.0 mm.

Fig. 5 Histogram plots of angle of long axis of garnet inclusion with respect to foliation in X-Z section (a) and to lineation in X-Y section (b).

Fig. 6 OC-images of garnet inclusions in X-Z section. (a), (b) Fine-grained Subspherical garnet inclusions. No subgrains are observed. (c) Pinch-and-swell structure of elongated garnet inclusion. This garnet is composed of three grains. (d) A single crystal elongated garnet inclusion. (e) Optical micrograph of coarse-grained garnet inclusion. (f) OC-image of coarse-grained garnet inclusion shown in Fig. 4(e). Coarse-grained garnet is commonly characterized by irregular interface and developed subgrains.

Fig. 7 (a) Plot of inclusion aspect ratio with respect to grain size, measured in X-Z section. R = grain size, L = aspect ratio. (b) Mean aspect ratios of garnet inclusions for

twelve groups (*R*: 10~50, 50~75, 75~100, 100~125, 125~150, 150~175, 175~200, 200~225, 225~250, 250~300, 300~400 and 400~600 μm). The detailed data are given in Table 1.

Fig. 8 Flinn plot of garnet inclusions, calculated from the mean aspect ration in X-Y and Y-Z section (solid circle). Numbers of inclusions for X-Y and Y-Z sections are 608 and 635, respectively. Squares indicate values for three groups divided by the length of intermediate axis of inclusions (Y<200, 200<Y<400, Y>400 μm).

Fig. 9 Garnet crystal preferred orientation (CPO). N = 319. Equal area projection, lower hemisphere. Contours in multiples of a uniform distribution (m.u.d.). Foliation (XY plane) is shown by a solid line and lineation (X) is horizontal within the plane of the foliation.

Fig. 10 Evolution of the aspect ratio (*L*) of inclusion by dislocation creep followed by eq. 15. The curves correspond to the differential stress of 0.1, 0.2, 0.4, 0.6, 0.8, 1.0 and

1.2 MPa, respectively.

Fig. 11 Evolution of the aspect ratio of inclusions (L) of size 50, 100, 150, 200, 300, 400, 500 and 600 μm. Calculated condition is $D_{gb} = 1.0 \times 10^{-12}$ m^2s^{-1} and $\sigma = 0.1$ MPa.

Fig. 12 Progressive evolutions of the aspect ratio (L) and grain size (R) distribution pattern for various magnitudes of the interface diffusion coefficient (1.0×10^{-10}, 1.0×10^{-11}, 1.0×10^{-12}, 1.0×10^{-13}, 1.0×10^{-14} m^2s^{-1}) and of differential stress (0.01, 0.1, 1.0 MPa).

Fig. 13 The L-R curves for the best-fitted conditions with five cases with different magnitudes of interface coefficients (1.0×10^{-10}, 1.0×10^{-11}, 1.0×10^{-12}, 1.0×10^{-13}, 1.0×10^{-14} m^2s^{-1}). The conditions of the calculations refer to Table 2 and Table 4. Solid square with error bar shows the observed L-R distribution of garnet inclusions from Skallen.

Fig. 14 (a) A framework of two stages of physical conditions (stage A, stage B) of shape development of garnet inclusions. (b) Progressive evolution of the *L*-*R* distribution pattern at stage A. (c) Progressive evolution of the *L*-*R* distribution pattern at stage B. At t = 14.4 My, the curve is fitted to the observed *L*-*R* pattern (solid squares with error bar).

Fig. 15 Absolute magnitudes of the rate of the change in the aspect ratio (year^{-1}) of garnet inclusion with respect to grain size (R) for the deformation history shown in Fig. 14: (a) t = 0, (b) t = 0.1, (c) t = 0.4, (d) t = 0.6, (e) t = 1.5, (f) t = 10.5 Myr. Bold broken line = dislocation component, fine broken line = diffusion creep component, solid line = rounding component. Conditions at stage A and B are σ_A = 1.0 MPa, $D_{gb,A}$ = 1.0 $\times 10^{-12}$ m^{2}s^{-1}, and σ_B = 0.014 MPa, $D_{gb,B}$ =1.0 $\times 10^{-11}$ m^{2}s^{-1}, respectively.

Table 1. Mean aspect ratios of garnet inclusions within twelve size ranges.

R : grain size (=(area/π)$^{0.5}$), N: number of inclusions, R_m : mean grain size, L_m : mean aspect ratio, sd: standard deviation of L_m .

R (m)	N	R_m	L_m	sd
10~50	119	30	0.828	0.09
50~75	212	62.5	0.773	0.13
75~100	177	87.5	0.700	0.15
100~125	106	112.5	0.577	0.17
125~150	90	137.5	0.519	0.17
150~175	80	162.5	0.497	0.17
175~200	47	187.5	0.444	0.19
200~225	48	212.5	0.390	0.13
225~250	24	237.5	0.417	0.14
250~300	39	275	0.420	0.18
300~400	37	350	0.453	0.16
400~600	26	500	0.454	0.19

Table 2. Parameters used in the calculation.

L	aspect ratio of inclusion	
R	grain size of inclusion [m]	
D_{gb}	interface diffusion coefficient [m^2/s]	
t	time [Myr]	
σ	differential stress [MPa]	
δ	width of grain boundary [m]	1.0×10^{-9}
Ω	volume of a vacancy [m^3]	1.0×10^{-30}
γ_s	interfacial tension between inclusion and host [N/m]	1.0
k	Boltzman' constant [JK^{-1}]	1.38×10^{-23}
T	temperature [K]	1223
A	constant	5
B	constant	9.5×10^{19} [a]
g	constant	36 *
	shear modulus [N/m]	9.5×10^{10} [a]
T_m	melting temperature [K]	1570 [a]
n	stress exponent	2.7 [a]

[a] Values are from *Karato et al.* , [1995].

Table 3. Magnitudes of strain rates of a garnet single crystal at T = 950 ˚C calculated by the constitutive equation of *Karato et al.* [1995] (eq. 14).

σ [MPa]	strain rate [s^{-1}]
0.01	1.17×10^{-19}
0.1	5.85×10^{-17}
0.2	3.80×10^{-16}
0.4	2.47×10^{-15}
0.6	7.38×10^{-15}
0.8	1.61×10^{-14}
1.0	2.93×10^{-14}
1.2	4.80×10^{-14}
10	1.47×10^{-11}
100	7.37×10^{-9}

Table 4. Magnitudes of differential stress and duration for the best-fitted curve for D_{gb} = 1.0 x10^{-10}, 1.0x10^{-11}, 1.0x10^{-12}, 1.0x10^{-13}, 1.0x10^{-14} m^2/s. ΔL^2 indicates the sum of the residuals calculated by eq. 17.

	D_{gb}	σ (MPa)	time (Myr)	ΔL^2
1	1.0 x 10^{-10}	0.014	13.8	0.001882
2	1.0 x 10^{-11}	0.019	20.0	0.018656
3	1.0 x 10^{-12}	0.039	20.0	0.086704
4	1.0 x 10^{-13}	1.7	0.1	0.063533
5	1.0 x 10^{-14}	1.7	0.1	0.028342

Fig. 1

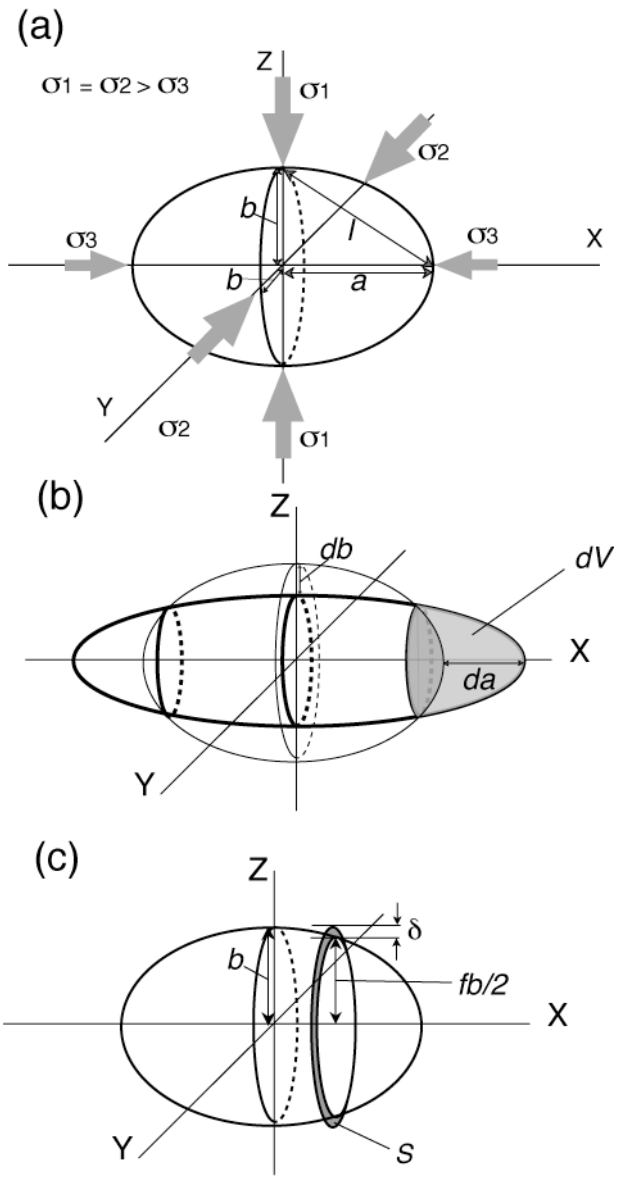

Fig. 2

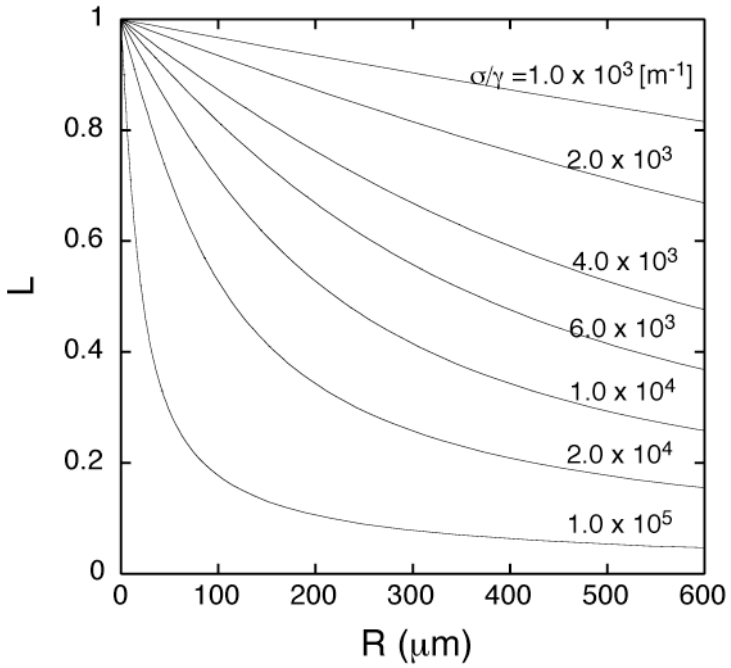
1
0.8
0.6
0.4
0.2
0
L
0
100
200
300
400
500
600
R (μm)
σ/γ =1.0 x 10^3 [m^-1]
2.0 x 10^3
4.0 x 10^3
6.0 x 10^3
1.0 x 10^4
2.0 x 10^4
1.0 x 10^5

Fig. 3

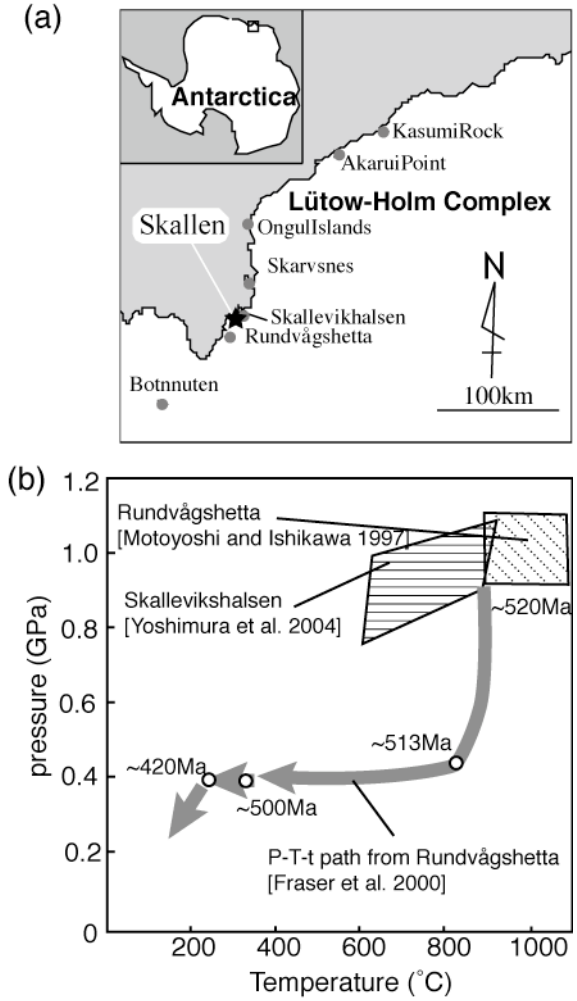
(a)
Antarctica
KasumiRock
AkaruiPoint
Lützow-Holm Complex
Skallen
OngulIslands
Skarvsnes
Skallevikhalsen
Rundvågshetta
Botnnuten
N
100km
(b)
Rundvågshetta
[Motoyoshi and Ishikawa 1997]
Skallevikshalsen
[Yoshimura et al. 2004]
~520Ma
~513Ma
~420Ma
~500Ma
P-T-t path from Rundvågshetta
[Fraser et al. 2000]
pressure (GPa)
Temperature (°C)
0
0.2
0.4
0.6
0.8
1.0
1.2
200
400
600
800
1000

Fig. 4

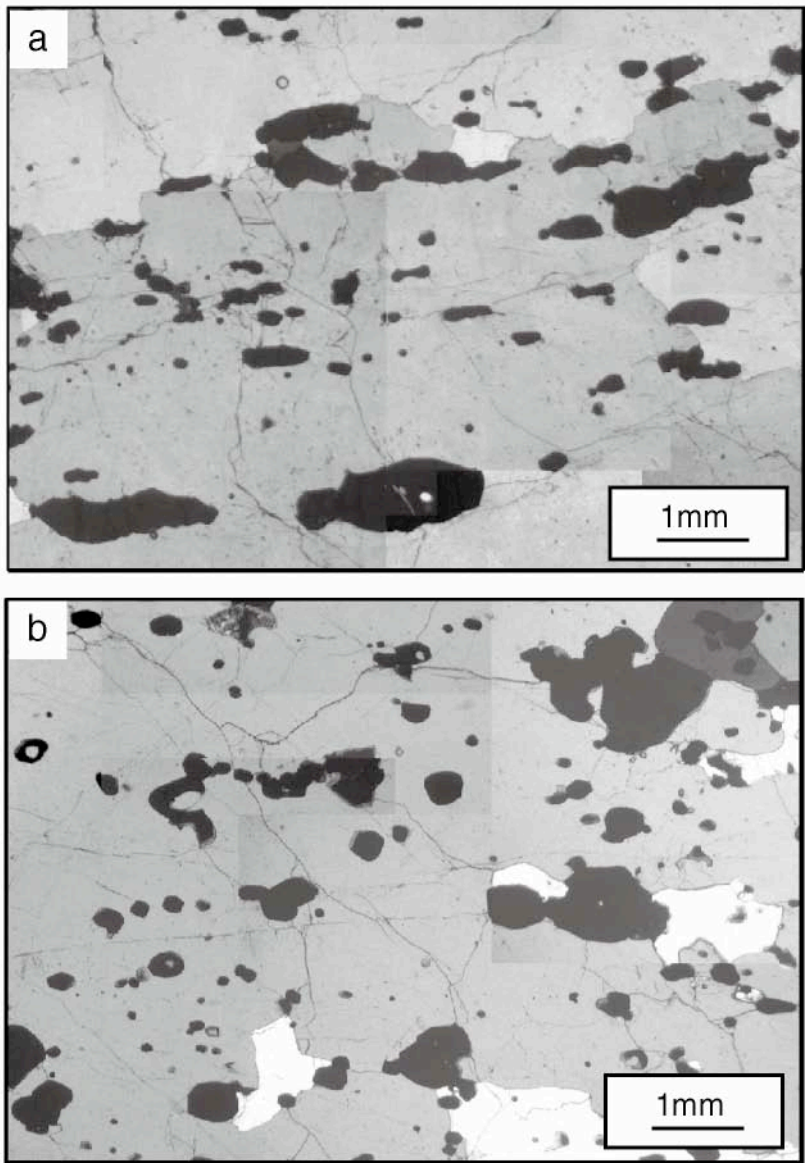

Fig. 5

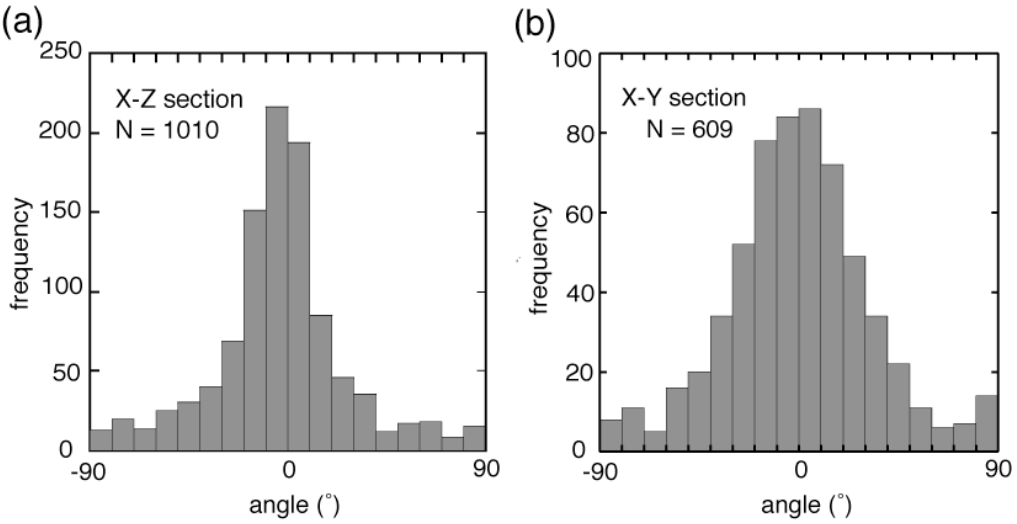
(a)
X-Z section
N = 1010
frequency
angle (˚)
(b)
X-Y section
N = 609
frequency
angle (˚)

Fig. 6

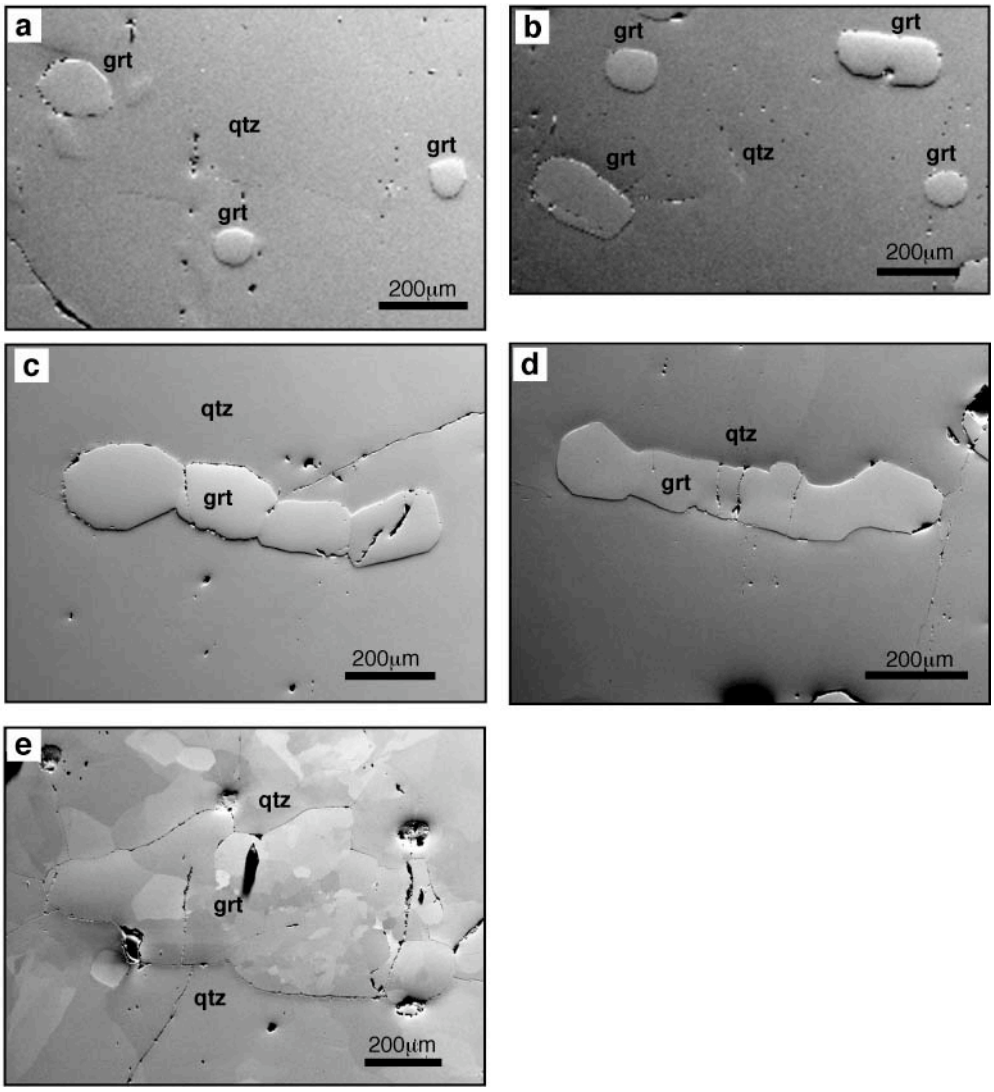
a
grt
qtz
grt
grt
200μm
b
grt
grt
grt
qtz
grt
200μm
c
qtz
grt
200μm
d
qtz
grt
200μm
e
qtz
grt
qtz
200μm

Fig. 7

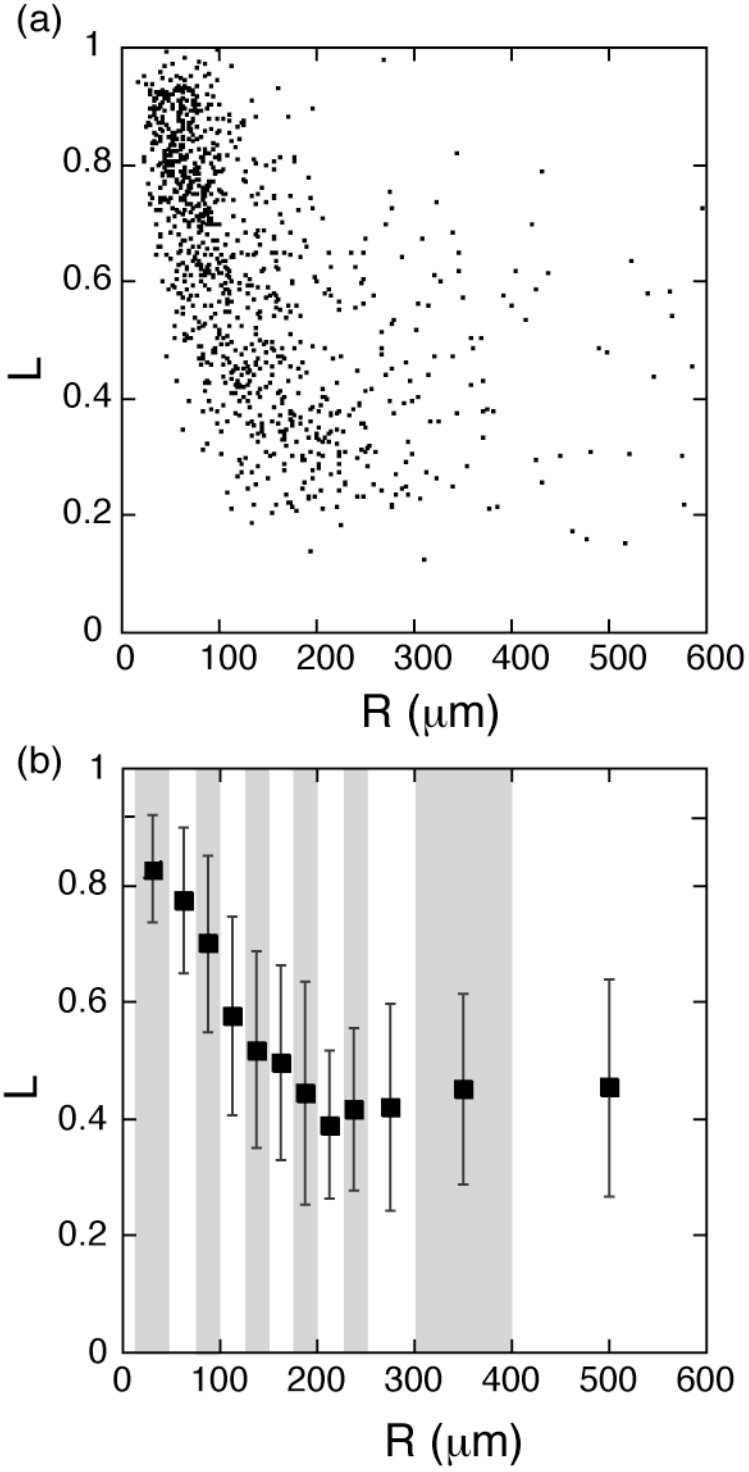
(a)
1
0.8
0.6
0.4
0.2
0
L
0
100
200
300
400
500
600
R (μm)
(b)
1
0.8
0.6
0.4
0.2
0
L
0
100
200
300
400
500
600
R (μm)

Fig. 8

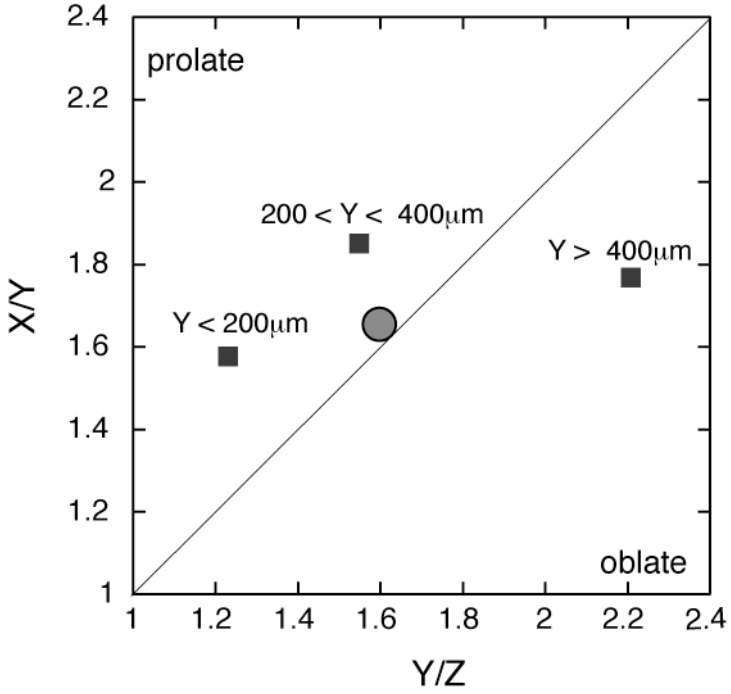
prolate
oblate
200 < Y < 400μm
Y > 400μm
Y < 200μm
X/Y
Y/Z
2.4
2.2
2
1.8
1.6
1.4
1.2
1
1
1.2
1.4
1.6
1.8
2
2.2
2.4

Fig. 9

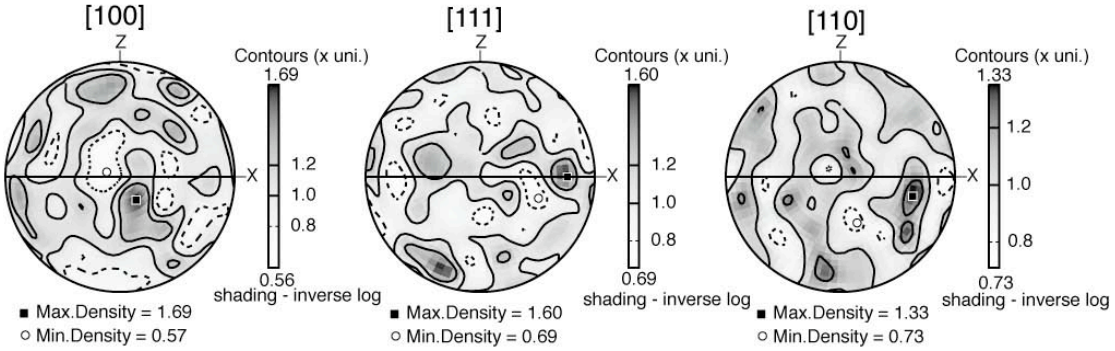
[100]
Z
X
Contours (x uni.)
1.69
1.2
1.0
0.8
0.56
shading - inverse log
■ Max.Density = 1.69
○ Min.Density = 0.57
[111]
Z
X
Contours (x uni.)
1.60
1.2
1.0
0.8
0.69
shading - inverse log
■ Max.Density = 1.60
○ Min.Density = 0.69
[110]
Z
X
Contours (x uni.)
1.33
1.2
1.0
0.8
0.73
shading - inverse log
■ Max.Density = 1.33
○ Min.Density = 0.73

Fig. 10

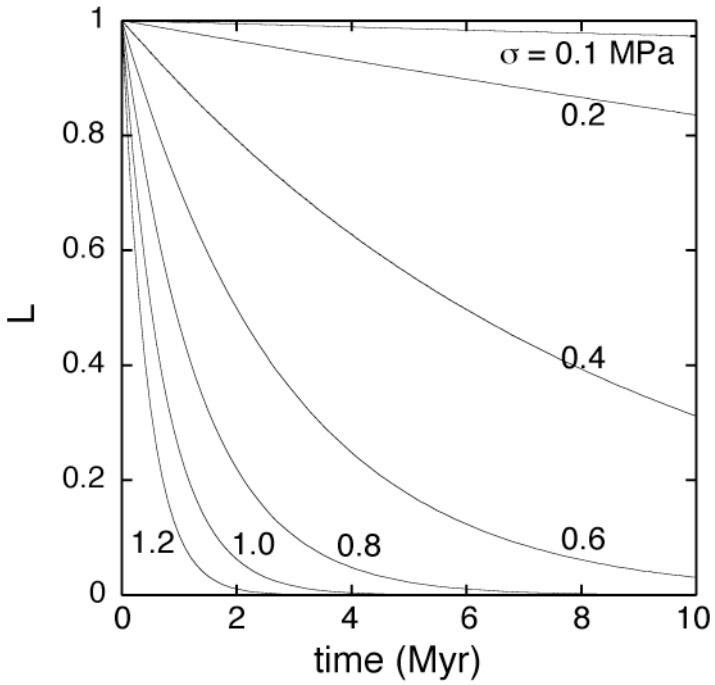
σ = 0.1 MPa
0.2
0.4
0.6
0.8
1.0
1.2
L
time (Myr)

Fig. 11

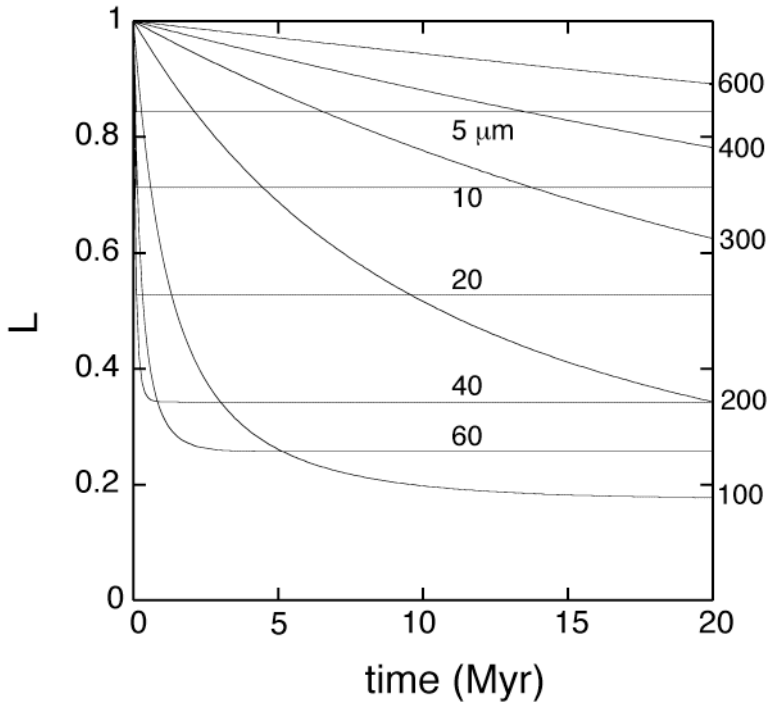
5 μm
10
20
40
60
600
400
300
200
100
L
time (Myr)

Fig. 12

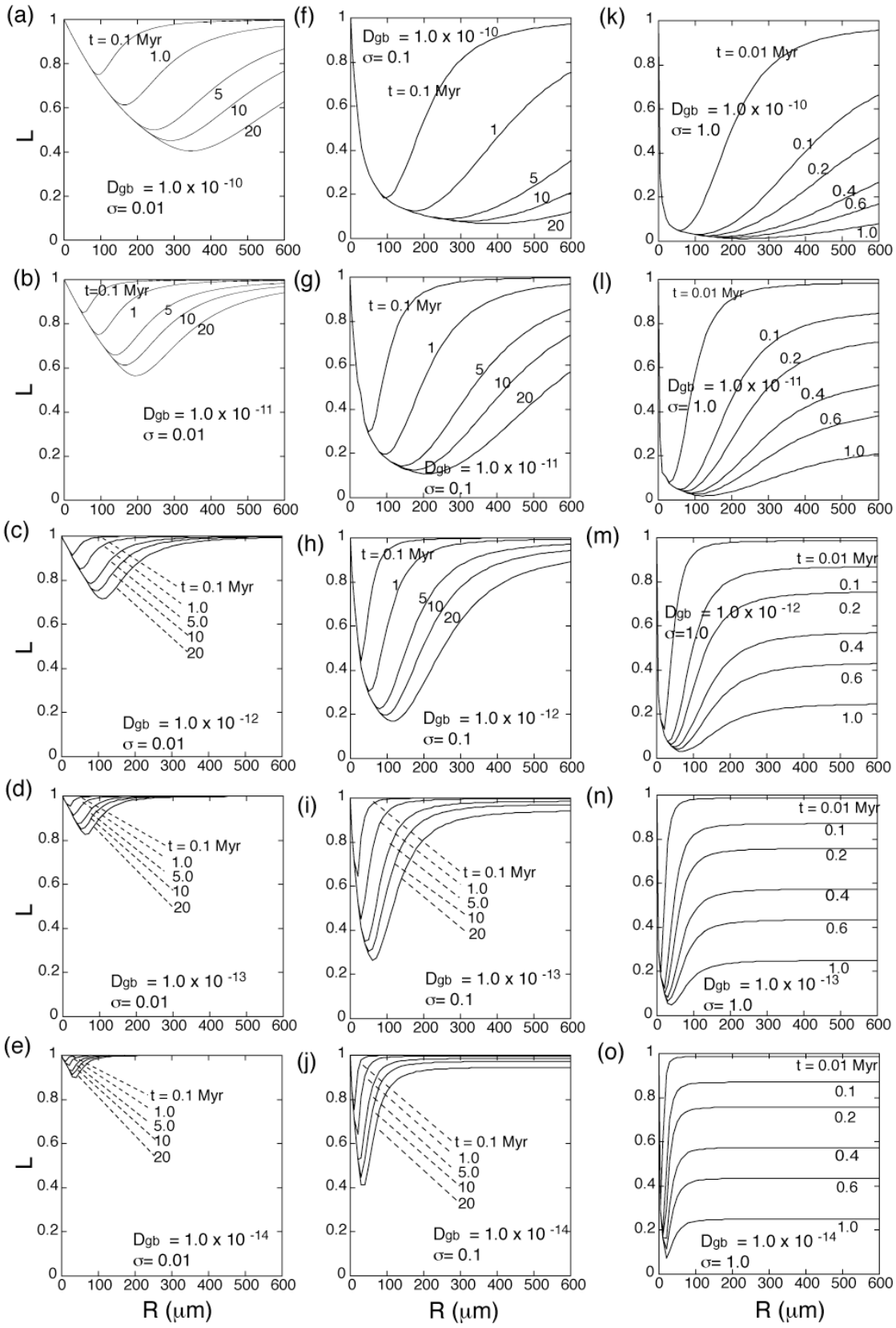
(a)
t = 0.1 Myr
1.0
5
10
20
Dgb = 1.0 x 10 -10
σ= 0.01
(f)
Dgb = 1.0 x 10 -10
σ= 0.1
t = 0.1 Myr
1
5
10
20
(k)
t = 0.01 Myr
Dgb = 1.0 x 10 -10
σ= 1.0
0.1
0.2
0.4
0.6
1.0
(b)
t=0.1 Myr
1
5
10
20
Dgb = 1.0 x 10 -11
σ = 0.01
(g)
t = 0.1 Myr
1
5
10
20
Dgb = 1.0 x 10 -11
σ= 0,1
(l)
t = 0.01 Myr
0.1
0.2
Dgb = 1.0 x 10 -11
σ= 1.0
0.4
0.6
1.0
(c)
t = 0.1 Myr
1.0
5.0
10
20
Dgb = 1.0 x 10 -12
σ = 0.01
(h)
t = 0.1 Myr
1
5
10
20
Dgb = 1.0 x 10 -12
σ= 0.1
(m)
t = 0.01 Myr
0.1
Dgb = 1.0 x 10 -12
σ=1.0
0.2
0.4
0.6
1.0
(d)
t = 0.1 Myr
1.0
5.0
10
20
Dgb = 1.0 x 10 -13
σ= 0.01
(i)
t = 0.1 Myr
1.0
5.0
10
20
Dgb = 1.0 x 10 -13
σ= 0.1
(n)
t = 0.01 Myr
0.1
0.2
0.4
0.6
1.0
Dgb = 1.0 x 10 -13
σ= 1.0
(e)
t = 0.1 Myr
1.0
5.0
10
20
Dgb = 1.0 x 10 -14
σ= 0.01
(j)
t = 0.1 Myr
1.0
5.0
10
20
Dgb = 1.0 x 10 -14
σ= 0.1
(o)
t = 0.01 Myr
0.1
0.2
0.4
0.6
1.0
Dgb = 1.0 x 10 -14
σ= 1.0
L
R (μm)
0
100
200
300
400
500
600
0.2
0.4
0.6
0.8
1

Fig. 13

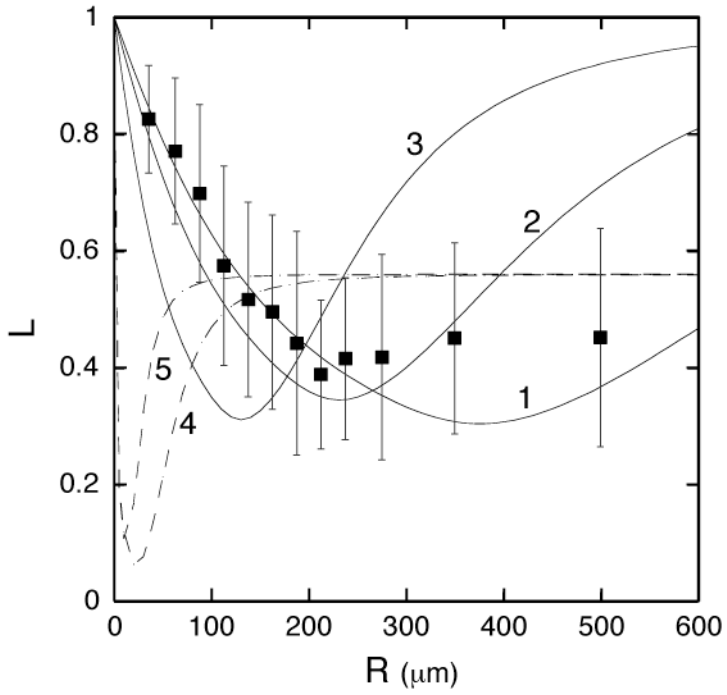

Fig. 14

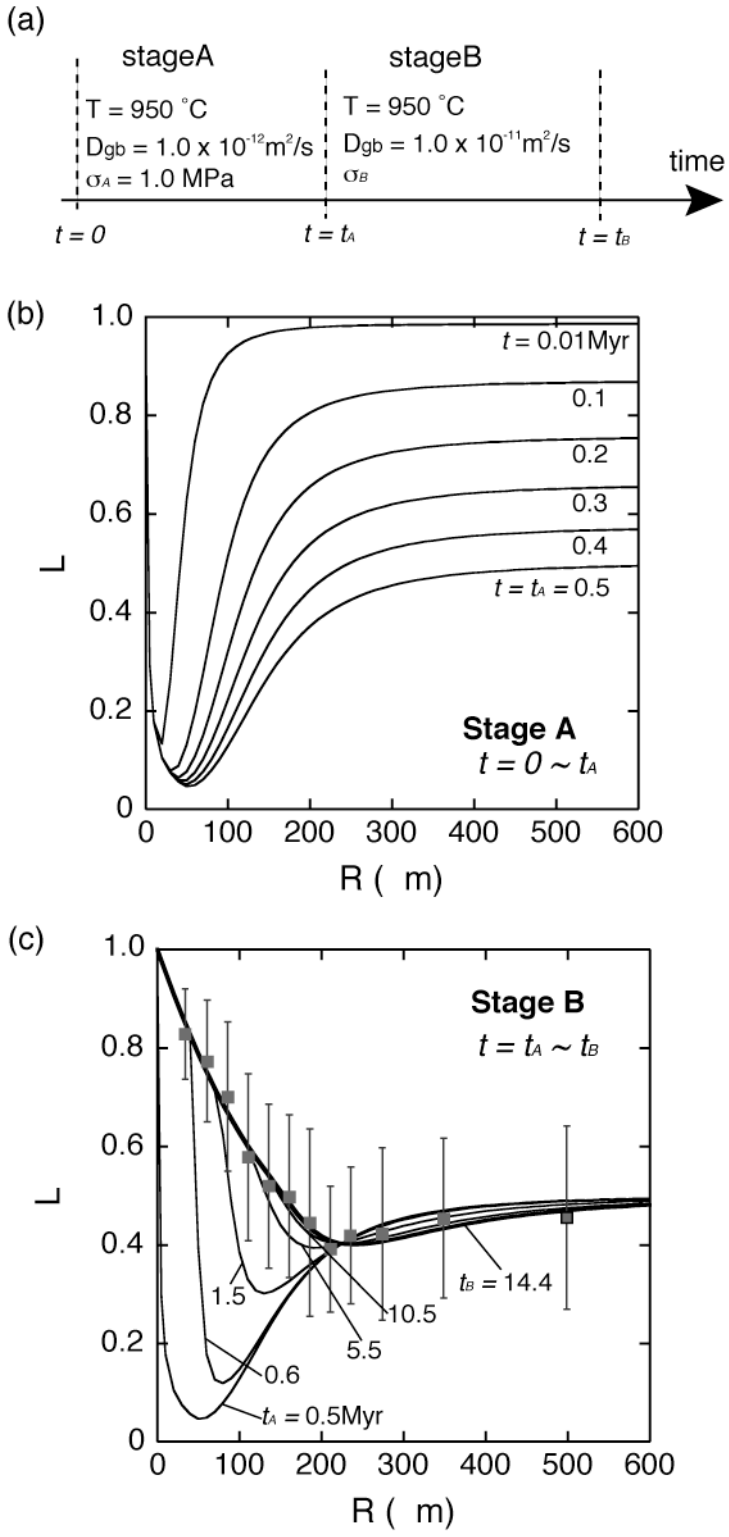
(a)
stageA
stageB
T = 950 ˚C
Dgb = 1.0 x 10-12m2/s
σA = 1.0 MPa
T = 950 ˚C
Dgb = 1.0 x 10-11m2/s
σB
time
t = 0
t = tA
t = tB
(b)
L
R (m)
t = 0.01Myr
0.1
0.2
0.3
0.4
t = tA = 0.5
Stage A
t = 0 ~ tA
(c)
L
R (m)
Stage B
t = tA ~ tB
1.5
0.6
tA = 0.5Myr
5.5
10.5
tB = 14.4

Fig. 15

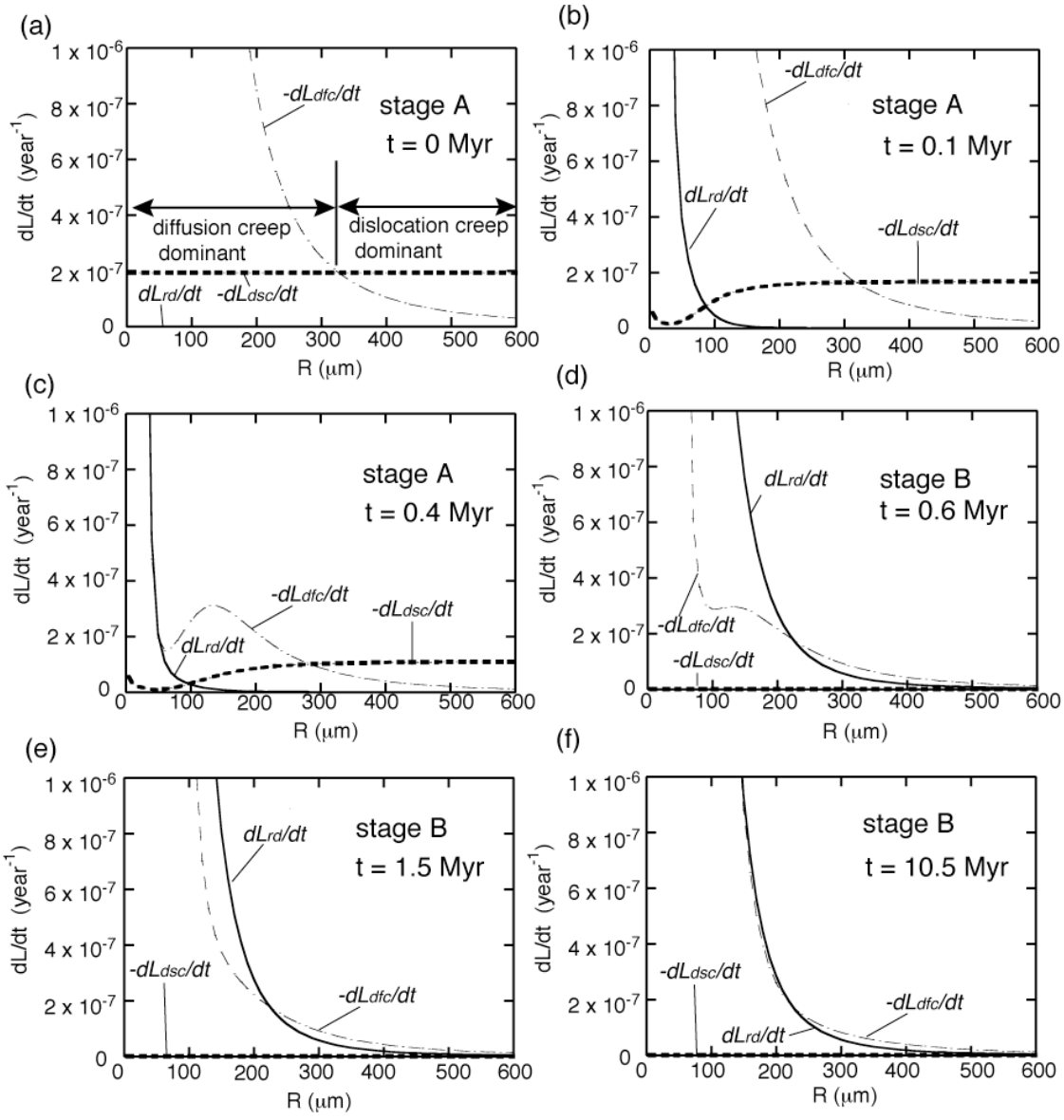
(a)
stage A
t = 0 Myr
-dLdfc/dt
diffusion creep dominant
dislocation creep dominant
dLrd/dt
-dLdsc/dt
(b)
stage A
t = 0.1 Myr
-dLdfc/dt
dLrd/dt
-dLdsc/dt
(c)
stage A
t = 0.4 Myr
-dLdfc/dt
-dLdsc/dt
dLrd/dt
(d)
stage B
t = 0.6 Myr
dLrd/dt
-dLdfc/dt
-dLdsc/dt
(e)
stage B
t = 1.5 Myr
dLrd/dt
-dLdsc/dt
-dLdfc/dt
(f)
stage B
t = 10.5 Myr
-dLdsc/dt
-dLdfc/dt
dLrd/dt
dL/dt (year-1)
R (μm)
1 x 10-6
8 x 10-7
6 x 10-7
4 x 10-7
2 x 10-7
0
0 100 200 300 400 500 600